JETP Letters, Vol. 71, No. 7, 2000, pp. 277–280. From Pis'ma v Zhurnal Éksperimental'noĭ i Teoreticheskoĭ Fiziki, Vol. 71, No. 7, 2000, pp. 401–406.

FIELDS, PARTICLES, AND NUCLEI

The $\omega(782) \longrightarrow 5\pi$ Decay[1]

N. N. Achasov and A. A. Kozhevnikov

Laboratory of Theoretical Physics, Sobolev Institute of Mathematics, Siberian Division, Russian Academy of Sciences, pr. Akademika Koptyuga 4, Novosibirsk-90, 630090 Russia

e-mail: achasov@math.nsc.ru

e-mail: kozhev@math.nsc.ru

Received March 6, 2000

The partial widths of the decays $\omega \longrightarrow 2\pi^+2\pi^-\pi^0$ and $\pi^+\pi^-3\pi^0$ are evaluated and their excitation curves in e^+e^- annihilation are obtained. © *2000 MAIK "Nauka/Interperiodica".*

PACS numbers: 13.25.Jx; 12.39.Fe; 11.30.Rd

At present, unconventional, from the point of view of the chiral pion dynamics, sources of soft pions are feasible. Indeed, the progress in increasing the luminosity of low-energy e^+e^- colliders (ϕ factories) [1] could offer naturally controlled sources of soft pions. Other possible source of such pions could be intense photon beams [2], provided sufficiently low invariant mass regions of the many-pion systems are isolated. The yield of pions is considerably enhanced when they are produced through proper vector resonance states. Then, choosing the many-pion decays of sufficiently low lying resonances, one can obtain soft pions in quantities sufficient for testing the predictions of chiral models that include vector mesons.

The decay $\omega(782) \longrightarrow 5\pi$ whose final-state pions possess the momenta $|\mathbf{q}_\pi| \simeq 74$ MeV, is just of this kind. The latter value is sufficiently small to expect the manifestation of chiral dynamics in the cleanest form. By this we mean that the higher derivative and loop terms in the effective Lagrangian are severely suppressed. The present paper is devoted to the evaluation of the partial width of this decay and plotting its excitation curve in e^+e^- annihilation.

The $\rho\pi$ sector is considered here on the basis of the Weinberg Lagrangian [3] revived later as the Lagrangian of hidden local symmetry (HLS) [4]. The former looks like

$$\mathcal{L} = -\frac{1}{4}(\partial_\mu\boldsymbol{\rho}_\nu - \partial_\nu\boldsymbol{\rho}_\mu + g[\boldsymbol{\rho}_\mu \times \boldsymbol{\rho}_\nu])^2 + \frac{m_\rho^2}{2}\left[\boldsymbol{\rho}_\mu + \frac{[\boldsymbol{\pi}\times\partial_\mu\boldsymbol{\pi}]}{2gf_\pi^2(1+\boldsymbol{\pi}^2/4f_\pi^2)}\right]^2 + \frac{(\partial_\mu\boldsymbol{\pi})^2}{2(1+\boldsymbol{\pi}^2/4f_\pi^2)^2} - \frac{m_\pi^2\boldsymbol{\pi}^2}{2(1+\boldsymbol{\pi}^2/4f_\pi^2)}, \quad (1)$$

where $\boldsymbol{\pi}$, m_π and $\boldsymbol{\rho}_\mu$, m_ρ stand for the isovector fields of π and ρ mesons and their masses, respectively, and $f_\pi = 92.4$ MeV is the pion decay constant. The cross stands for the vector product of the isovector quantities defined on the isotopic space. The $\rho\rho\rho$ coupling constant g and the $\rho\pi\pi$ coupling constant $g_{\rho\pi\pi}$ are related to the ρ mass and pion decay constant f_π via the parameter of hidden local symmetry a as [4]

$$g = m_\rho/f_\pi\sqrt{a}, \quad g_{\rho\pi\pi} = \sqrt{a}m_\rho/2f_\pi. \quad (2)$$

Note that $a = 2$ if one demands that the universality condition $g = g_{\rho\pi\pi}$ be satisfied. Then the so-called Kawarabayashi–Suzuki–Riazzuddin–Fayyazuddin relation $2g_{\rho\pi\pi}^2 f_\pi^2/m_\rho^2 = 1$ [5] arises, which beautifully agrees with experiment. The $\rho\pi\pi$ coupling constant resulting from this relation is $g_{\rho\pi\pi} = 5.89$. The inclusion of the interaction of the $\omega(782)$ with the $\rho\pi$ state is achieved upon adding the term induced by the anomalous Lagrangian of Wess and Zumino [4, 6],

$$\mathcal{L}_{\omega\rho\pi} = \frac{N_c g^2}{8\pi^2 f_\pi}\varepsilon_{\mu\nu\lambda\sigma}\partial_\mu\omega_\nu(\boldsymbol{\pi}\cdot\partial_\lambda\boldsymbol{\rho}_\sigma), \quad (3)$$

where ω_ν stands for the ω meson field and $N_c = 3$ is the number of colors.

One may convince oneself that the $\omega \longrightarrow \rho\pi \longrightarrow 5\pi$ decay amplitude unambiguously results from the Weinberg Lagrangian (1) and the anomaly-induced Lagrangian (3). This amplitude is represented by the diagrams shown in Fig. 1. Its general expression is expected to be cumbersome. However, it can be considerably simplified upon noting that the small pion momenta permit one to use the nonrelativistic expressions

[1] This article was submitted by the authors in English.

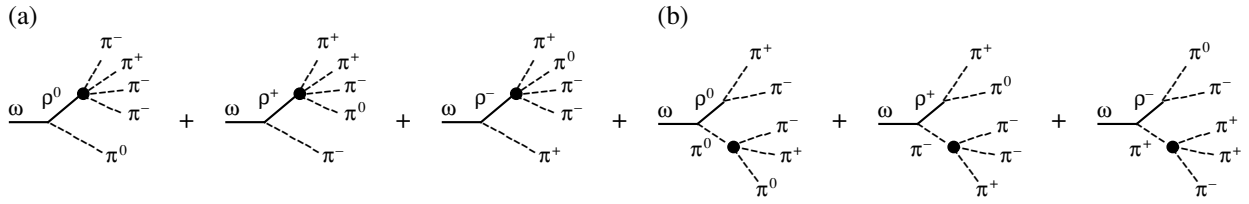

Fig. 1. The diagrams describing the amplitudes of the decay $\omega \longrightarrow \pi^+\pi^-\pi^+\pi^-\pi^0$. The shaded circles in set (a) refer to the whole $\rho \longrightarrow 4\pi$ amplitudes Eq. (5). The shaded circles in set (b) refer to the effective $\pi \longrightarrow 3\pi$ vertices given by Eq. (6). The symmetrization over momenta of identical pions is meant. The diagrams for the decay $\omega \longrightarrow \pi^+\pi^-\pi^0\pi^0\pi^0$ are obtained from those shown upon the evident replacements.

$$
\begin{aligned}
M[\rho^0 &\longrightarrow \pi^+(q_1)\pi^+(q_2)\pi^-(q_3)\pi^-(q_4)] \\
&\simeq -\frac{g_{\rho\pi\pi}}{2f_\pi^2}(\varepsilon, q_1+q_2-q_3-q_4), \\
M[\rho^0 &\longrightarrow \pi^-(q_1)\pi^-(q_2)\pi^0(q_3)\pi^0(q_4)] \\
&\simeq -\frac{g_{\rho\pi\pi}}{4f_\pi^2}(\varepsilon, q_1-q_2), \\
M[\rho^+ &\longrightarrow \pi^+(q_1)\pi^+(q_2)\pi^-(q_3)\pi^0(q_4)] \\
&\simeq \frac{g_{\rho\pi\pi}}{4f_\pi^2}(\varepsilon, q_1+q_2-2q_4), \\
M[\rho^+ &\longrightarrow \pi^+(q_1)\pi^0(q_2)\pi^0(q_3)\pi^0(q_4)] \\
&\simeq \frac{g_{\rho\pi\pi}}{f_\pi^2}(\varepsilon, q_1)
\end{aligned}
\qquad (4)
$$

for the $\rho \longrightarrow 4\pi$ decay amplitudes in the diagrams of Fig. 1a. Here ε, q_A ($A = 1, 2, 3, 4$) stand for the ρ meson polarization and pion momentum four-vectors.[2] The above expressions are valid with an accuracy of 5% in the 4π mass range relevant for the present purpose. Likewise, the expression for the combination $D_\pi^{-1} M(\pi \longrightarrow 3\pi)$ standing in the expression for the diagrams in Fig. 1b can be replaced, with the same accuracy, by $-(8m_\pi^2)^{-1}$ times the nonrelativistic $\pi \longrightarrow 3\pi$ amplitudes. The latter look like

$$
\begin{aligned}
M(\pi^+ &\longrightarrow \pi^+\pi^+\pi^-) = -2m_\pi^2/f_\pi^2, \\
M(\pi^+ &\longrightarrow \pi^+\pi^0\pi^0) = -m_\pi^2/f_\pi^2, \\
M(\pi^0 &\longrightarrow \pi^+\pi^-\pi^0) = -m_\pi^2/f_\pi^2, \\
M(\pi^0 &\longrightarrow \pi^0\pi^0\pi^0) = -3m_\pi^2/f_\pi^2.
\end{aligned}
\qquad (5)
$$

Note that, in the nonrelativistic limit, the $\rho \longrightarrow 4\pi$ decay amplitudes depend on the HLS parameter a only through an overall factor $g_{\rho\pi\pi}/f_\pi^2 = \sqrt{a}\, m_\rho/2f_\pi^3$, whereas the $\pi \longrightarrow 3\pi$ amplitudes do not depend on it at all.

Yet even the simplified expressions for the $\omega \longrightarrow 5\pi$ amplitudes are not easy to use for evaluation of the branching ratios. To go further, one should note the following. The invariant mass of the 4π system, on which the contribution of the diagrams shown in Fig. 1a depends, changes in very narrow range 558 MeV $< m_{4\pi} <$ 642 MeV. Hence, one can set it in all the ρ propagators, to an accuracy of 20% in width, to the equilibrium value $\overline{m_{4\pi}^2}^{1/2} = 620$ MeV evaluated for the pion energy $E_\pi = m_\omega/5$, which gives the dominant contribution. The same is true for the invariant mass of the pion pairs, on which the ρ propagators entering the diagrams Fig. 1b depend. This mass varies in the narrow range 280 MeV $< m_{2\pi} <$ 360 MeV. With the same accuracy, one can set it to $\overline{m_{2\pi}^2}^{1/2} = 295$ MeV in all relevant propagators. On the other hand, the amplitude of the process $\omega \longrightarrow \rho^0\pi^0 \longrightarrow (2\pi^+2\pi^-)\pi^0$ corresponding to the first diagram in Fig. 1a is

$$
\begin{aligned}
&M_{\omega \to \rho^0\pi^0 \to (2\pi^+2\pi^-)\pi^0} \\
&= 4\frac{N_c g_{\rho\pi\pi} g^2}{8(2\pi)^2 f_\pi^3}\varepsilon_{\mu\nu\lambda\sigma} q_\mu \epsilon_\nu (q_1+q_2)_\lambda \frac{q_{4\sigma}}{D_\rho(q-q_4)},
\end{aligned}
\qquad (6)
$$

where the momentum assignment is $\pi^+(q_1)\pi^+(q_2)\pi^-(q_3)\pi^-(q_5)\pi^0(q_4)$. Hereafter, q_μ, ϵ_μ stand for the four-vectors of momentum and polarization, respectively, of the $\omega(782)$ and

$$
D_\rho(q) = m_\rho^2 - q^2 - im_\rho^2\left(\frac{s-4m_\pi^2}{m_\rho^2-4m_\pi^2}\right)^{3/2}\frac{\Gamma_{\rho\pi\pi}(m_\rho)}{\sqrt{q^2}} \qquad (7)
$$

is the inverse propagator of the $\rho(770)$. The other relevant amplitude corresponding to the first diagram in Fig. 1b is

[2] Our notation for the scalar product of two-vectors a and b is $(a, b) = a_0b_0 - \mathbf{ab}$.

$$M_{\omega\to\rho^0\pi^0\to(\pi^+\pi^-)(\pi^+\pi^-\pi^0)} = \frac{N_c g_{\rho\pi\pi} g^2}{8(2\pi)^2 f_\pi^3} \times \varepsilon_{\mu\nu\lambda\sigma} q_\mu \epsilon_\nu (1+P_{12})(1+P_{35}) \frac{q_{1\lambda} q_{3\sigma}}{D_\rho(q_1+q_3)}, \quad (8)$$

where P_{ij} interchanges the momenta q_i and q_j. Then, taking into account the above consideration concerning the invariant masses, one can show that

$$M_{\omega\to 2\pi^+2\pi^-\pi^0} \approx \frac{5}{2} M_{\omega\to\rho^0\pi^0\to(2\pi^+2\pi^-)\pi^0}\left[1 - \frac{D_\rho(\overline{m^2_{4\pi}})}{2D_\rho(\overline{m^2_{2\pi}})}\right]. \quad (9)$$

The same treatment shows that

$$M_{\omega\to\pi^+\pi^-3\pi^0} \approx \frac{5}{2} M_{\omega\to\rho^+\pi^-\to(\pi^+3\pi^0)\pi^-}\left[1 - \frac{D_\rho(\overline{m^2_{4\pi}})}{2D_\rho(\overline{m^2_{2\pi}})}\right], \quad (10)$$

where

$$M_{\omega\to\rho^+\pi^-\to(\pi^+3\pi^0)\pi^-} = -4\frac{N_c g_{\rho\pi\pi} g^2}{8(2\pi)^2 f_\pi^3} \frac{\varepsilon_{\mu\nu\lambda\sigma} q_\mu \epsilon_\nu q_{1\lambda} q_{2\sigma}}{D_\rho(q-q_2)} \quad (11)$$

and the momentum assignment is $\pi^+(q_1)\pi^-(q_2)\pi^0(q_3)\pi^0(q_4)\pi^0(q_5)$. The second term in square brackets of Eqs. (9) and (10) approximates the contribution of the diagrams shown in Fig. 1b. The numerical values of $\overline{m^2_{4\pi}}^{1/2}$ and $\overline{m^2_{2\pi}}^{1/2}$ found above are such that the correction factor in parentheses of Eqs. (9) and (10) amounts to 20% in magnitude. In what follows, the above correction will be taken into account as an overall factor of 0.64 in front of the branching ratios of the decays ω ⟶ 5π. When making this estimate, the imaginary part of the ρ propagators in square brackets of Eqs. (9) and (10) is neglected. This assumption is valid to an accuracy better than 1% in width.

The evaluation of the partial widths valid to an accuracy of 20% can be obtained upon taking the amplitude of each considered decay as 5/2 times the ρπ production state amplitude with the subsequent decay ρ ⟶ 4π, and calculate the partial width of the latter with the help of Eq. (5). One obtains

$$B_{\omega\to 2\pi^+2\pi^-\pi^0} = \left|1 - \frac{D_\rho(\overline{m^2_{4\pi}})}{2D_\rho(\overline{m^2_{2\pi}})}\right|^2 \left(\frac{5}{2}\right)^2 \frac{2}{\pi\Gamma_\omega} \times \int_{4m_{\pi^+}}^{m_\omega - m_{\pi^0}} dm \frac{m^2 \Gamma_{\omega\to\rho^0\pi^0}(m)\Gamma_{\rho\to 2\pi^+2\pi^-}(m)}{|D_\rho(m^2)|^2} = 1.1\times 10^{-9}, \quad (12)$$

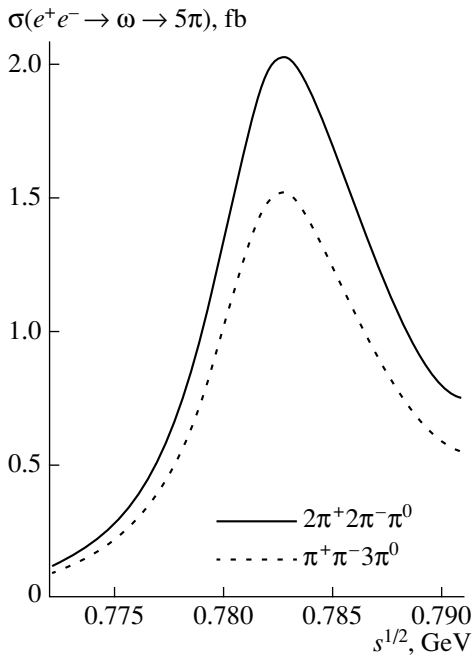

Fig. 2. The ω ⟶ 5π excitation curves in e^+e^- annihilation in the vicinity of the ω resonance.

where $\Gamma_{\omega\to\rho^0\pi^0}(m) = g^2_{\omega\rho\pi} q^3(m_\omega, m, m_{\pi^0})/12\pi$ and $g_{\omega\rho\pi} = N_c g^2/8\pi^2 f_\pi = 14.3\ \text{GeV}^{-1}$. Note also the a^{-1} dependence of the ω ⟶ 5π width on the HLS parameter a. The branching ratio $B_{\omega\to\pi^+\pi^-3\pi^0}$ is obtained from Eq. (12) upon inserting the lower integration limit to $m_{\pi^+} + 3m_{\pi^0}$, $m_{\pi^0} \longrightarrow m_{\pi^+}$ in the expression for the momentum q and substitution of the $\rho^+ \longrightarrow \pi^+3\pi^0$ decay width corrected for the mass difference of charged and neutral pions. Of course, the main correction of this sort comes from the phase-space volume of the final 4π state. One obtains

$$B_{\omega\to\pi^+\pi^-3\pi^0} = 8.5\times 10^{-10}. \quad (13)$$

As is pointed out in [4], the inclusion of the direct $\omega \longrightarrow \pi^+\pi^-\pi^0$ vertex reduces the 3π decay width of ω by 33%. This implies that one should use the suppression factor ≃0.75 instead of 0.64, which results in the increase of the above branching ratios by a factor of 1.17.

The numerical value of the ω ⟶ 5π decay width changes by a factor of two when varying the energy within $\pm\Gamma_\omega/2$ around the ω mass. In other words, the dependence of this partial width on energy is very strong. This is illustrated in Fig. 2, where the ω ⟶ 5π excitation curves in e^+e^- annihilation are plotted. The mentioned strong energy dependence of the partial width results in the asymmetric shape of the ω resonance and the shifting of its peak by +0.7 MeV. As is seen from Fig. 2, the peak value of the 5π-state produc-

tion cross section is about 1.5–2.0 femtobarns. Yet the decays $\omega \longrightarrow 5\pi$ can be observable on e^+e^- colliders. Indeed, with the luminosity $L = 10^{33}$ c^{-2} s^{-1} near the ω peak, which seems to be feasible, one may expect about two events per week for the considered decays to be detected at these colliders.

The strong energy dependence of the five-pion partial width of ω implies that the branching ratio at the ω mass $B_{\omega \to 5\pi} = \Gamma_{\omega \to 5\pi}/\Gamma_\omega$, evaluated above is slightly different from that determined by the expression

$$B^{\text{aver}}_{\omega \to 5\pi}(E_1, E_2) = \frac{2}{\pi}\int_{E_1}^{E_2} dE \frac{E^2 \Gamma_\omega B_{\omega \to 5\pi}(E)}{(E^2 - m_\omega^2)^2 + (m_\omega \Gamma_\omega)^2}. \quad (14)$$

Taking $E_1 = 772$ MeV and $E_2 = 792$ MeV, one finds $B^{\text{aver}}_{\omega \to 2\pi^+2\pi^-\pi^0}(E_1, E_2) = 9.0 \times 10^{-10}$ and $B^{\text{aver}}_{\omega \to \pi^+\pi^-3\pi^0}(E_1, E_2) = 6.7 \times 10^{-10}$ to be compared to Eqs. (12) and (13), respectively. In particular, the quantity $B^{\text{aver}}_{\omega \to 2\pi^+2\pi^-\pi^0}(E_1, E_2)$ is the relevant characteristic of this specific decay mode in photoproduction experiments. The Jefferson Lab "photon factory" [2] could also be suitable for detecting five-pion decays of ω. However, in view of the suppression of the ω photoproduction cross section by a factor of 1/9, as compared with the ρ one, the total number of ω mesons will amount to 7×10^8 per nucleon. Hence, an increase in the intensity of this machine by a factor of 50 is highly desirable in order to observe the decay $\omega \longrightarrow 5\pi$ and measure its branching ratio. Evidently, ω photoproduction on heavy nuclei is preferable in view of the dependence of the cross section on the atomic weight A growing as $A^{0.8–0.95}$ [7].

Together with the e^+e^- annihilation experiments, the study of the photoproduction of the five-pion states on heavy nuclei would also allow one to measure the corresponding partial width of ω(782). The comparison with theoretical expectations presented here would give the possibility of testing the predictions of chiral models in the situation where the decay amplitudes are determined by very low pion momenta.

We are grateful to G.N. Shestakov for discussions. This work was supported in part by the Russian Foundation for Basic Research and INTAS IR-97-232.

REFERENCES

1. A. N. Skrinsky, in *Proceedings of the Workshop on Physics and Detectors for DAPhiNE'95, Frascati, 1995*, Ed. by R. Baldini, F. Bossi, G. Capon, *et al.*, Frascati Physics Series, Vol. IV, p. 3; G. Vignola, *ibid.*, p. 19.
2. A. R. Dzierba, in *Proceedings from Jefferson Lab/NCSU, Workshop on Hybrids and Photoproduction Physics, North Carolina State University, 1997*, p. 661.
3. S. Weinberg, Phys. Rev. **166**, 1568 (1968).
4. M. Bando, T. Kugo, S. Uehar, *et al.*, Phys. Rev. Lett. **54**, 1215 (1985); M. Bando, T. Kugo, and K. Yamawaki, Nucl. Phys. B **259**, 493 (1985); Prog. Theor. Phys. **73**, 1541 (1985); Phys. Rep. **164**, 217 (1988).
5. K. Kawarabayashi and M. Suzuki, Phys. Rev. Lett. **16**, 255 (1966); Riazzuddin and Fayyazuddin, Phys. Rev. **147**, 1071 (1966).
6. J. Wess and B. B. Zumino, Phys. Lett. B **37**, 95 (1971).
7. D. W. G. S. Leith, in *Hadronic Interactions of Electrons and Photons* (Academic, New York, 1971), p. 195.

JETP Letters, Vol. 71, No. 7, 2000, pp. 281–284. Translated from Pis'ma v Zhurnal Éksperimental'noĭ i Teoreticheskoĭ Fiziki, Vol. 71, No. 7, 2000, pp. 407–411.

ATOMS, SPECTRA, AND RADIATION

Spectral Broadening of Femtosecond Laser Pulses in Fibers with a Photonic-Crystal Cladding

A. B. Fedotov*, A. M. Zheltikov*, L. A. Mel'nikov, A. P. Tarasevitch***, and D. von der Linde*****

** International Laser Center, Physics Faculty, Moscow State University, Vorob'evy gory, Moscow, 119899 Russia*
e-mail: zheltikov@nls1.ilc.msu.su
*** Saratov State University, Saratov, 410026 Russia*
**** Institut für Laser- und Plasmaphysik, Universität Essen, Essen, D-45117 Germany*

Received January 26, 2000

Changes in the spectra of femtosecond laser pulses propagating through fibers with a cladding having the structure of a two-dimensional photonic crystal are experimentally investigated. It is demonstrated that the waveguide properties of defect modes of photonic-crystal fibers provide an opportunity to considerably increase the efficiency of spectral broadening of short laser pulses as compared with conventional fibers. *© 2000 MAIK "Nauka/Interperiodica".*

PACS numbers: 42.65.Wi; 42.70.Qs

Fibers with a photonic-crystal cladding [1–4] are a new type of optical waveguides whose unique properties are of special interest in the context of the possibility of solving many urgent problems of modern optics. The cladding in fibers of this type has the structure of a two-dimensional (2D) photonic crystal (PC); i.e., it consists of a 2D periodic array of closely packed hollow silica fibers. Due to the periodic arrangement of air holes in a silica fiber, the transmission spectrum of such a structure displays photonic band gaps (PBGs), i.e., frequency ranges where radiation with certain directions of the wave vector cannot penetrate into the fiber cladding. If a fiber without a hole is used to make the core of such a structure, then the missing hole can be considered as a defect in a 2D photonic-crystal lattice. Such fibers seem to offer much promise for extending many ideas of the physics of photonic crystals [5–7] to the optical range.

Knight *et al.* [1] were the first to fabricate fibers with a PBG cladding (which were later called holey fibers) and to investigate the properties of such fibers. These studies have shown that fibers of this type support a single-mode propagation regime within a broad spectral range, allowing radiation energy losses to be considerably reduced in the single-mode regime and the effective area of the waveguide mode to be substantially increased. These properties of PBG fibers seem to hold much promise for enhancing the efficiency of nonlinear-optical interactions. Some nonlinear-optical applications of such fibers have recently been discussed by Broderick *et al.* [4].

In this letter, we present the results of experimental studies devoted to the propagation of femtosecond laser pulses in holey fibers. Our experiments demonstrate that the use of such fibers allows the efficiency of spectral broadening of femtosecond pulses to be considerably increased as compared with conventional fibers. This finding may have important implications in pulse compression and creation of new efficient broadband radiation sources. Furthermore, the results of our experiments confirm the possibility of enhancing the efficiency of nonlinear-optical interactions of ultrashort light pulses in defect modes of PC structures.

The technology employed to fabricate holey fibers was similar to the procedure described by Knight *et al.* [1, 2]. Holey fibers were fabricated by repeating a procedure of stacking thin glass capillaries into a periodic array and then fusing the stack and drawing this structure at high temperatures. The initial inner diameter of the glass capillaries used in this process was about 1 mm. The above-described procedure allowed us to fabricate fibers where the cladding had the structure of a 2D photonic crystal with periodically arranged air holes. By changing the conditions of the fabrication process, we were able to vary the final inner diameter of air holes in the PBG cladding from 0.56 to 12.8 μm. A defect was introduced into a 2D PC lattice by replacing one of the capillaries by a conventional fiber, which was made of different glass in our case. This central fiber served as a core in a holey fiber (Fig. 1). The pitch of the PBG structure in the cladding of fibers employed in our experiments ranged from 1.4 to 32 μm.

The idea of enhancing the efficiency of nonlinear-optical interactions and, consequently, the efficiency of spectral broadening and supercontinuum generation in holey fibers with respect to conventional fibers is based

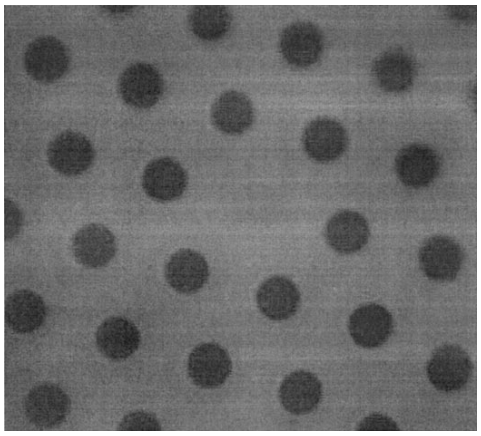

Fig. 1. A microscope image of a cut of a holey fiber with a pitch of the PBG cladding equal to 32 μm.

on robust low-loss single-mode waveguiding, which is supported, as demonstrated by Knight *et al.* [1, 2], by holey fibers within a broad frequency range, and local-field enhancement, which is characteristic of defect modes of PBG structures [6–8]. Although the wavelength of laser radiation lay relatively far from the photonic band gap of the PBG cladding in our experiments, the light-field confinement in the fiber core, as indicated by the results of our measurements, resulted in a detectable increase in the efficiency of spectral broadening of short laser pulses as compared with conventional fibers.

Experiments on spectral broadening in holey fibers were carried out with the use of a laser system consisting of a Ti : sapphire laser, an eight-pass preamplifier, and a four-pass final amplifier. This laser system generated 150-fs pulses with a repetition rate of 10 Hz. The maximum energy of these pulses was as high as 100 mJ. In holey-fiber experiments, the energy of laser pulses was varied within the range from 1 to 15 μJ. The contrast ratio of femtosecond pulses measured at 1 ps from the pulse maximum was estimated as 10^{-4}.

The laser beam was focused on the entrance end of a holey fiber with a lens L1 (Fig. 2). Measurements were performed with lenses with different focal lengths. In particular, to be able to compare spectral broadening in holey and conventional supercontinuum-generating fibers, we carried out measurements using a 10-cm-focal-length lens L1, which focused a light beam into a 100-μm spot. For holey fibers with core sizes ranging from 0.56 to 1.28 μm, this regime of focusing corresponded to excitation of the waveguide mode in a nearly plane wave (this regime of excitation of defect modes in photonic crystals was theoretically investigated in [8]). Only a small fraction of light energy was coupled into the waveguide mode under these conditions, while a considerable part of the light beam was scattered due to the roughness of the fiber end. The spectra of light pulses at the output of the holey fiber were analyzed with the use of a monochromator and a CCD camera, which was used to image the output slit of the monochromator (Fig. 2).

Analysis of the spectra of light coming out of the fiber reveals considerable spectral broadening of femtosecond pulses in a PBG waveguide. Starting with a transform-limited 150-fs pulse of a Ti : sapphire laser with an energy of 1.5 μJ (Fig. 3a), we observed spectral broadening of the pulse at the output of the fiber, allowing a spectral width of about 40 nm at the level of 0.3 of the maximum intensity to be achieved for pulses with a moderate intensity. Note that a considerable fraction of the radiation energy was contained in the wings of the spectrum under these conditions (Fig. 3b). The insets in Figs. 3a and 3b show the CCD images of a laser beam at the output of the monochromator, with the horizontal direction corresponding to the spatial beam profile and the vertical direction corresponding to

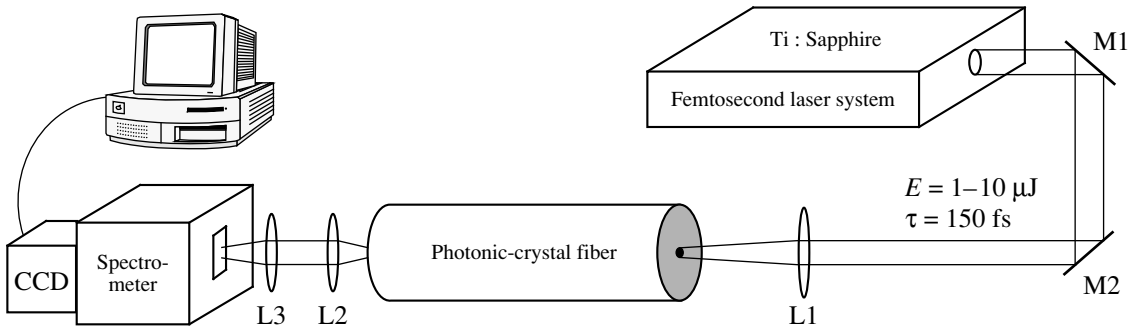

Fig. 2. Diagram of the experimental setup employed to investigate the spectral broadening of femtosecond pulses in holey fibers: L1–L3, lenses; M1, M2, mirrors.

the spectral profile of a laser pulse. The spectral broadening of femtosecond pulses coming out of a holey fiber is manifested as the increase in the vertical sizes of CCD images. The image shown in the inset in Fig. 3b also indicates the presence of irregular modulation in the spectrum of a femtosecond pulse at the output of a holey fiber.

The main features of spectral broadening of femtosecond pulses observed in our experiments are similar to the features of the spectral broadening of short pulses in conventional fibers. The properties of such phenomena are well understood now and are described in detail in the extensive literature (e.g., see [9]). Importantly, even with considerable losses due to scattering, spectral broadening of femtosecond pulses in a holey fiber was much more efficient than in a conventional silica fiber with a much higher quality of the entrance end.

The results of our experiments allow us to conclude that, in accordance with our expectations, PBG-cladding fibers allow the efficiency of nonlinear-optical interactions to be considerably increased. The fact that holey fibers can be employed to increase the efficiency of supercontinuum generation seems to be very important for practical applications. Supercontinuum-generating sources are currently employed more and more extensively for various spectroscopic applications [10]. Since supercontinuum generation involves nonlinear-optical processes, high intensities of incident light are usually required to ensure supercontinuum emission with sufficient spectral brightness. The results presented in this paper demonstrate that an efficient way of generating supercontinuum is to use optical fibers with a PBG cladding, which ensure large propagation lengths due to robust waveguiding within a broad frequency range and may considerably reduce the requirements for the intensity of incident radiation in supercontinuum generation.

The experiments described above demonstrate efficient spectral broadening of 150-fs pulses of a Ti : sapphire laser in optical fibers with PBG cladding. This effect can be employed for pulse compression and the creation of new sources of broadband radiation. While the advantages of using holey fibers for improving the efficiency of nonlinear-optical interactions have been demonstrated by our experiments quite clearly, the efficiency of nonlinear-optical processes in holey fibers can be further improved by using wavelengths lying closer to the photonic band gap of the PC cladding, employing materials with higher nonlinearities for the fabrication of PBG structures, and improving phase matching by separately controlling different components of PBG-fiber dispersion [11].

We are grateful to V.I. Beloglazov and Yu.S. Skibina for the fabrication of composite fibers and to A.N. Naumov, D.A. Sidorov-Biryukov, and A.V. Tarasishin for useful discussions.

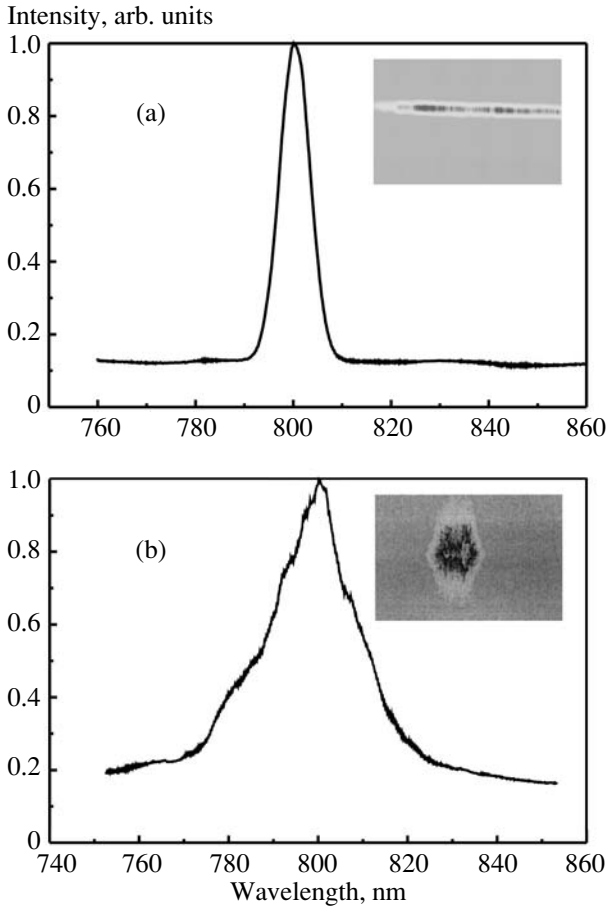

Fig. 3. Spectral broadening of a femtosecond light pulse in a holey fiber: (a) the spectrum of a 150-fs Ti : sapphire laser output pulse and (b) the broadened spectrum of the pulse at the output of the holey fiber with a pitch of the PBG cladding equal to 1.7 μm. The insets show the images of the beam patterns recorded by a CCD camera, with the horizontal direction corresponding to the spatial beam profile and the vertical direction corresponding to the spectral profile of the laser pulse.

This study was supported in part by the President of the Russian Federation Grant no. 00-15-99304, INTAS project no. 97-0369, and the Russian Foundation for Basic Research project no. 00-02-17567.

REFERENCES

1. J. C. Knight, T. A. Birks, P. St. J. Russell, and D. M. Atkin, Opt. Lett. **21**, 1547 (1996).
2. J. C. Knight, T. A. Birks, R. F. Cregan, *et al.*, Opt. Mater. **11**, 143 (1999).
3. P. J. Bennett, T. M. Monro, and D. J. Richardson, Opt. Lett. **24**, 1203 (1999).
4. N. G. R. Broderick, T. M. Monro, P. J. Bennett, and D. J. Richardson, Opt. Lett. **24**, 1395 (1999).
5. E. Yablonovitch, J. Opt. Soc. Am. B **10**, 283 (1993).

6. J. Joannopoulos, R. Meade, and J. Winn, *Photonic Crystals* (Princeton Univ., Princeton, 1995); *Photonic Band Gaps and Localization*, Ed. by C. M. Soukoulis (Plenum, New York, 1993).

7. N. I. Koroteev, S. A. Magnitskiĭ, A. V. Tarasishin, and A. M. Zheltikov, Opt. Commun. **159**, 191 (1999); A. M. Zheltikov, S. A. Magnitskiĭ, and A. V. Tarasishin, Zh. Éksp. Teor. Fiz. (2000) (in press); A. M. Zheltikov, Lectures of the Basic Optics and Spectroscopy Education and Research Center (Basic Optics and Spectroscopy Education and Research Center, Moscow, 1999), Issue 2, p. 79.

8. A. M. Zheltikov, S. A. Magnitskiĭ, and A. V. Tarasishin, Pis'ma Zh. Éksp. Teor. Fiz. **70**, 323 (1999) [JETP Lett. **70**, 323 (1999)]; S. A. Magnitskiĭ, A. V. Tarasishin, and A. M. Zheltikov, Appl. Phys. B **69**, 497 (1999).

9. F. Salin, J. Watson, J. F. Cormier, *et al.*, Springer Ser. Chem. Phys. **55**, 306 (1992).

10. *Femtosecond Laser Pulses*, Ed. by C. Rulliere (Springer, Berlin, 1998).

11. A. M. Zheltikov, N. I. Koroteev, and A. N. Naumov, Zh. Éksp. Teor. Fiz. **115**, 1561 (1999) [JETP **88**, 857 (1999)].

Translated by A. Zheltikov

JETP Letters, Vol. 71, No. 7, 2000, pp. 285–288. Translated from Pis'ma v Zhurnal Éksperimental'noĭ i Teoreticheskoĭ Fiziki, Vol. 71, No. 7, 2000, pp. 412–417.

PLASMA, GASES

Hierarchical Pattern of Superdiffusion

A. I. Olemskoĭ

Sumy State University, Sumy, 244007 Ukraine

e-mail: olemskoi@ssu.sumy.ua

Received February 23, 2000

Under the assumption of slow evolution of the cluster structure of walker positions, the kinetic equation is derived, according to which the Lévy law is fulfilled on the mesoscopic time-scale, while the system tends to the generalized Tsallis distribution on the macroscopic time-scale. The asymptotics are found for the time dependences of the hierarchy characteristic scale and the probability distribution over the hierarchical levels.

PACS numbers: 05.40.Fb; 05.45.Of

As is known, stochastic transfer processes are the generalization of the diffusion process [1]. They are characterized by the transition from the ordinary square-root law to the relation

$$\langle \mathbf{r}^2 \rangle \propto t^{2/z}, \tag{1}$$

with the dynamic exponent $z \neq 2$ ($\mathbf{r}$ is the coordinate of a walking particle and t is time). For subdiffusion in the presence of traps, the jump mean waiting time diverges, $\langle t \rangle = \infty$, as a result of which the jumps occur discretely in space and the transfer process is decelerated ($z > 2$). It accelerates ($z < 2$) in the presence of Lévy flights when the particle executes jumps of arbitrary length with the divergent mean square displacement $\langle \mathbf{x}^2 \rangle = \infty$ at discrete time instants.

A remarkable feature of the superdiffusion process is that the successive positions of the walking particle form a cluster structure representing a fractal set with the dimension of exponent z [2]. Since the fractal is formed by the hierarchical construction, one can assume that the behavior of the stochastic system is determined not only by the particle displacement in the real space but also by a much slower evolution of the clusters of its successive positions. This evolution is known to amount to diffusion over the sites of a hierarchical tree in the ultrametric space.

This study is devoted to the description of superdiffusion as a random walk in the real and ultrametric spaces. The generalized Fokker–Planck equation will be used to show that the particle positions conform to the Lévy distribution on the mesoscopic time-scale, where the cluster structure does not undergo noticeable changes. Similar to the slow relaxation of spin glasses, it should be expected that on the macroscopic time-scale the cluster structure would undergo noticeable changes on the way to the stationary distribution of particle positions. Such behavior results in the Tsallis form of asymptotic distribution, which, in turn, corresponds to the highest level of the particle-position cluster distribution [3].

Let us first present the information necessary for the description of superdiffusion in the case when the cluster structure is ignored [4]. The initial kinetic equation has the form

$$P(\mathbf{r}, t + \tau_0) - P(\mathbf{r}, t) = \int [f(\mathbf{r}, \mathbf{r}')P(\mathbf{r}', t) - f(\mathbf{r}', \mathbf{r})P(\mathbf{r}, t)]\, d\mathbf{r}', \tag{2}$$

where τ_0 is the jump time and $f(\mathbf{r}, \mathbf{r}')$ is the probability of transition from point $\mathbf{r}'$ to point $\mathbf{r}$. At $t \gg \tau_0$, the left-hand side of Eq. (2) amounts to the time derivative $\dot{P}(\mathbf{r}, t)$, and it is convenient, under the assumption of spatial homogeneity, to pass over to integration with respect to the displacement $\mathbf{x} \equiv \mathbf{r} - \mathbf{r}'$ on the right-hand side. Then, using the detailed balancing principle $f(\mathbf{x}) = f(-\mathbf{x})$, one can recast the kinetic equation in the form

$$\tau_0 \dot{P}(\mathbf{r}, t) = \int [P(\mathbf{r} + \mathbf{x}, t) - P(\mathbf{r}, t)]\, f(\mathbf{x})\, d\mathbf{x}.$$

Taking into account the normalization condition $\int_{-\infty}^{\infty} f(\mathbf{x})\, d\mathbf{x} = 1$ for the space Fourier transforms, one obtains $\tau_0 \dot{P}_{\mathbf{k}}(t) = -(1 - f_{\mathbf{k}})P_{\mathbf{k}}(t)$, where $\mathbf{k} \longrightarrow 0$ is the wave vector multiplied by the real-space characteristic scale. In superdiffusion processes, of crucial importance is the behavior of the transition probability at large distances, $f(\mathbf{x}) \sim |\mathbf{x}|^{-(d+z)}$, where d is the space dimensionality. In the corresponding $\mathbf{k} \longrightarrow 0$ limit, the $1 - f_{\mathbf{k}}$ factor is reduced to $D_z|\mathbf{k}|^z$, where D_z is the effective diffusion coefficient whose explicit expression is determined by the $f(\mathbf{x})$ function (in particular, for $d = 1$, it was found that $D_z = 2^{-z}\Gamma(1 - z/2)/\Gamma(1 + z/2)$, where $\Gamma(\xi)$

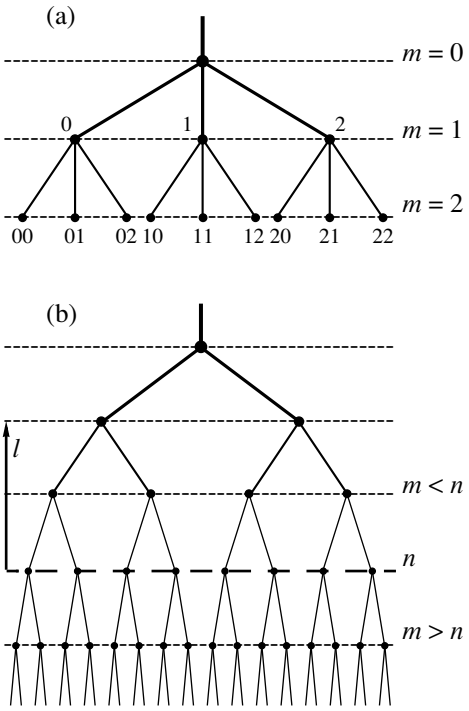

Fig. 1. Simplest hierarchical trees: (a) tree parametrization with the branching ratio $s = 3$ and (b) bifurcation tree, $s = 2$.

is the gamma function [4]). As a result, one arrives at the Lévy distribution

$$P_{\mathbf{k}}(t) = P_{\mathbf{k}}(0)\exp(-t/\tau_{\mathbf{k}}), \quad \tau_{\mathbf{k}} \equiv D_z^{-1}|\mathbf{k}|^{-z}\tau_0, \qquad (3)$$

characterized by the mesoscopic time $\tau_{\mathbf{k}} \gg \tau_0$. The corresponding kinetic equation in the real space contains a fractional derivative of order z.

When the cluster structure is taken into account, the probability density $P_{\mathbf{u}}(\mathbf{r}, t)$ and the transition intensities $f_{\mathbf{uu}'}(\mathbf{r}, \mathbf{r}')$ in kinetic equation (2) become dependent on the ultrametric coordinate $\mathbf{u}$ [5]. To reveal this dependence, let us consider a regular hierarchical tree characterized by a fixed branching ratio $s > 1$ and the number $n \gg 1$ of hierarchy levels. In this case, the ultrametric coordinate $\mathbf{u}$ is an n-valued number in the s-digit number system: $\mathbf{u} \equiv u_0u_1\ldots u_m\ldots u_{n-1}$, $u_m = 0, 1, \ldots, s-1$ (an example is shown in Fig. 1a). Accordingly, the transition intensity is written as a power series

$$f_{\mathbf{uu}'} = \sum_{m=0}^{n} f(u_m - u'_m)s^{n-m},$$

where the first term ($m = 0$) corresponds to the highest hierarchy level governing the behavior of the whole system, while the last term ($m = n$) corresponds to the lowest level representing the smallest clusters. By definition, the distance between the points $\mathbf{u}$ and $\mathbf{u}'$ is $0 \le l \le n$ if the conditions $u_m = u'_m$ are fulfilled for $m = 0, 1, \ldots, n - (l + 1)$ but $u_m \neq u'_m$ for $m = n - 1, n - l + 1, \ldots, n$ [6]. For this reason, at a fixed distance l, the first $n - l$ terms of the above series are zero by definition, while the last l terms contain the s^{n-m} multiplier, which, in the continuous limit $s \gg 1$, is much smaller than the s^l multiplier in the first of the remaining terms. As a result, the term corresponding to $m = n - l$: $f_{\mathbf{uu}'} \sim s^l = s^{n-m}$ is the only leading term of the power series under consideration. Similarly, one can show that the probability density $P_{\mathbf{u}} \sim s^{n-l} = s^m$. Upon passing from the regular to the arbitrary tree [7], the branching ratio s becomes the variable quantity and, according to the above estimates, the transition intensities $f_{\mathbf{uu}'} \longrightarrow f(n-m)$ and the probability density $P_{\mathbf{ku}} \longrightarrow P_{\mathbf{k}}(m)$ take the form of a Mellin transform:

$$f(n-m) \equiv \int_0^\infty f(s)s^{n-m}ds, \quad P_{\mathbf{k}}(m) \equiv \int_0^\infty P_{\mathbf{k}}(s)s^m ds, \quad (4)$$

where $f(s)$ and $P(s)$ are the respective weight functions.

The kinetic equation allowing for the cluster structure has the form

$$\tau_{\mathbf{k}}\dot{P}_{\mathbf{k}}(n, t) = \sum_{m>n} f(m-n)P_{\mathbf{k}}(n, t) - \sum_{m<n} f(n-m)P_{\mathbf{k}}(m, t). \qquad (5)$$

Here, the first term on the right-hand side allows for the hierarchical interrelation between the nodes of the lower levels $m > n$ through a given n, while the subtracted term allows for the interrelation of a given level n through the upper levels $m < n$ (see Fig. 1b). In deriving Eq. (5), the adiabatic approximation was used because, the particle walks occur much more rapidly than do the cluster structure changes on a macroscopic time-scale τ (see below). Expanding $P_{\mathbf{k}}(m, t)$ in $n - m$ to the quadratic term, one obtains the following equation in the continuous limit $n \gg 1$:

$$\tau_{\mathbf{k}}\dot{P}_{\mathbf{k}}(n, t) = \frac{\partial}{\partial n}\left[F(n)P_{\mathbf{k}}(n, t) - \frac{\partial}{\partial n}D(n)P_{\mathbf{k}}(n, t)\right] + \mathcal{D}P_{\mathbf{k}}(n, t), \qquad (6)$$

where the moments

$$F(n) \equiv \sum_{m<n}(n-m)f(n-m),$$

$$2D(n) \equiv \sum_{m<n}(n-m)^2 f(n-m)$$

and the quantity

$$\mathcal{D} \equiv \sum_{m>n} f(m-n) - \sum_{m<n} f(n-m) \tag{7}$$

specifying the difference between the rates of establishing hierarchical interrelation through the upper and lower levels are introduced.

The restrictions $m > n$ and $m < n$ are usually absent in the summation over the system states in Eq. (7), so that $\mathcal{D} = 0$ [8]. However, it is beyond reason to formulate such a condition for hierarchical systems, where the rate of establishing the interrelation essentially depends on the levels (upper or lower) mediating this process. Such is the case because the ultrametric space is inhomogeneous, as is evident from its geometric imaging (Fig. 1). For this reason, the following ansatz (the basic assumption) is adopted in this work:

$$\mathcal{D} \equiv -\epsilon q P_{\mathbf{k}}^{q-1}(n, t)\frac{\partial}{\partial n}, \tag{8}$$

where q and ϵ are positive parameters. This ansatz is formally justified by the fact that the integral $\int \mathcal{D} P dn$ is reduced within a factor of $-\epsilon(q-1)$ to the Jackson derivative with exponent $\alpha_q = (q-1)\ln P/\ln q$ [9]. As distinct from the ordinary derivative corresponding to the $q \longrightarrow 1$ limit, the Jackson derivative determines the rate of changing the $P(n)$ function not upon the argument shift $dn \longrightarrow 0$ but upon its dilatation qn and, therefore, provides the basis for an analysis of self-similar systems. From the physical point of view, the fact that the difference $\mathcal{D}$ between the rates of establishing the hierarchical interrelation depends on the probability density $P_{\mathbf{k}}(n, t)$ implies the existence of a nonlinear feedback, which, as is seen from what follows, is responsible for the nonadditivity. Substitution of Eq. (8) in Eq. (6) results in the following kinetic equation of superdiffusion:

$$\tau_{\mathbf{k}}\dot{P}_{\mathbf{k}}(n, t) = \frac{\partial}{\partial n} \times \left\{ [F(n)P_{\mathbf{k}}(n, t) - \epsilon P_{\mathbf{k}}^{q}(n, t)] - \frac{\partial}{\partial n} D(n) P_{\mathbf{k}}(n, t) \right\}. \tag{9}$$

Compared to the ordinary systems [8], the opposite signs of the diffusion and linear-drift terms are noteworthy; this is caused by the choice of the opposite signs in initial Eq. (5). This sign difference is due to the fact that the autonomous hierarchical (e.g., bureaucratic) systems are not decomposed but spontaneously reproduced [7]. Note also that the nonlinearity of Eq. (9) does not allow one to use Mellin transform (4), as was done for the Fourier transform of Eq. (2).

Turning to an analysis of Eq. (9), let us first consider the case $F(n) = 0$ and $D(n) = \text{const}$, when the nonlinear drift term dominates. The respective stationary probability distribution

$$P(n) = A\left(\frac{D}{\epsilon} + (q-1)(n+1)\right)^{-1/(q-1)}, \quad A \equiv (2-q)\left(\frac{D}{\epsilon} + (q-1)\right)^{(2-q)/(q-1)} \tag{10}$$

increases monotonically with decreasing n, i.e., with growth of the cluster of walker positions, and transforms to the Tsallis distribution at the highest level $n = 0$ corresponding to the whole system [3]. Using the generalized definition of entropy, it is easy to show that distribution (10) at $q \neq 1$ corresponds to the nonadditive statistical system for which the $q < 1$ and $q > 1$ cases are equivalent [9]. As will be seen below, the first case corresponds to the infinitely growing asymptotic of the probability density, and therefore it will be assumed that $q > 1$.

In the nonstationary case, the analytical description can be carried out in the self-similar regime, when the system behavior is determined by the time dependence $n_c(t)$ of the characteristic hierarchy scale, while the probability distribution is represented by a homogeneous function $P(n, t) = n_c^{\alpha}(t)\pi(\nu)$, $\nu \equiv n/n_c$ [10]. If the normalization condition

$$\int_0^{\infty} P(n, t) dn = 1,$$

is satisfied, the leading contribution comes from the drift term caused by the inhomogeneity of the ultrametric space. Then, the exponent $\alpha = -1$, and the self-similar regime is established if the condition $n_c^{q-1}\dot{n}_c = \text{const} \equiv C/\tau_{\mathbf{k}}$ and the equation $(\epsilon q\pi^{q-1} - C\nu)\pi' - C\pi = 0$ are satisfied (hereafter, the prime means differentiation with respect to the corresponding argument). The solution has the form $\pi^{q-1} = (C/\epsilon)\nu$ and is valid for times $t \ll \tau_d$, where $\tau_d \equiv (\epsilon^{q-2}/D^{q-1})n^q\tau_{\mathbf{k}}$. When the drift and the diffusion contributions are of the same order ($t \sim \tau_d$), the normalization of the distribution over hierarchical levels breaks down [2] and the conditions $\alpha(q-1) + 1 = 0$, $n_c\dot{n}_c = C/\tau_{\mathbf{k}}$ and the equation $D\pi'' + (\epsilon q\pi^{q-1} - C\nu)\pi' + \alpha C\pi = 0$ must be satisfied to ensure the self-similar regime. The corresponding solution has asymptotics $\pi^{q-1} \longrightarrow (q-1)^{-1}(D/\epsilon)\nu^{-1}$ at $\nu \longrightarrow 0$ and $\pi^{q-1} \longrightarrow (2C/q\epsilon)\nu$ at $\nu \longrightarrow \infty$. The first asymptotic occurs at large times $t \gg \tau$, $\tau \equiv (n^2/C)\tau_{\mathbf{k}}$ and the second one occurs at small times $t \ll \tau$.

Thus, for $F(n) = 0$ and $D(n) = \text{const}$, the contribution of the diffusion term at the initial stage $t \ll \tau_d$ is negligibly small, so that the distribution over the levels is normalized by the ordinary condition. In this case, the characteristic hierarchy scale increases with time fol-

lowing the power law $n_c^q = qC(t/\tau_{\mathbf{k}})$ (the lower levels become increasingly substantial), while the probability density decreases hyperbolically, $P^{q-1}(n, t) = (n/q\epsilon)(t/\tau_{\mathbf{k}})^{-1}$: the lower the level, the more rapid the decrease (it also follows from this that $q > 1$). The transition to the diffusion stage proceeds rapidly for higher levels and results in the modification of the time dependence $n_c(t)$ to the ordinary square-root form $n_c = \sqrt{2C(t/\tau_{\mathbf{k}})}$ at $\tau_d \sim t \ll \tau$, but the probability density decreases hyperbolically as at the initial stage. With further time increase to macroscopic values $t \gg \tau$, the $n_c(t)$ dependence remains unchanged and the probability distribution assumes the asymptotic form $P^{q-1}(n) \longrightarrow (q-1)^{-1}(D/\epsilon)n^{-1}$ corresponding to the stationary distribution (10) at $n \gg D/\epsilon$.

In the presence of an external force $F(n) = \text{const}$ and the multiplicative noise [$D(n) \neq \text{const}$], the above-mentioned behavior is realized only at small times $t \ll n(F - D')^{-1}\tau_{\mathbf{k}}$. If the opposite condition $n + (F - D')(t/\tau_{\mathbf{k}}) \gg [\epsilon/(F - D')]^{1/(q-1)}$ is fulfilled, the characteristic scale increases linearly, $n_c = C(t/\tau_{\mathbf{k}})$, and the probability decreases as $P(n, t) = [n + (F - D')(t/\tau_{\mathbf{k}})]^{-1}$. The stationary distribution takes the exponential form $P(n) \propto D^{-1}\exp\{\int (F/D)\,dn\}$, which, however, does not mean the presence of additivity. Indeed, since the same dependence $D(n)$ governs the diffusion process for both the whole system and its parts, the condition of multiplicativity of probabilities breaks down: $P_{1,2}(n) = D(n)P_1(n)P_2(n)$, where the subscripts indicate the macroscopic components. Therefore, the system with the multiplicative noise is nonadditive even with the Boltzmann definition of entropy.[1]

[1] Note that the term "multiplicative noise" bears no relation to the property of multiplicativity of the corresponding probabilities but reflects the fact that the noise originates from the fluctuation of the kinetic coefficient of the force acting on the system.

The above analysis demonstrates that superdiffusion of a hierarchical system free of external action ($F = 0$) proceeds nonadditively. An assumption of this sort is at the basis of the works of Tsallis *et al.* [see 9], where the nonadditivity is postulated in the definition of the transition probabilities $f(\mathbf{x})$ and, moreover, the Fokker–Planck equation is assumed to be nonlinear. With the approach proposed in this paper, both nonlinearity and nonlinearity-induced nonadditivity result from the hierarchical structure. This allows the conclusion to be drawn that free hierarchical systems are invariably nonadditive.

I am grateful to C. Tsallis for kindly placing the results on nonadditive systems at my disposal.

REFERENCES

1. J.-P. Bouchaud and A. Georges, Phys. Rep. **195**, 127 (1990).
2. D. H. Zanette, Braz. J. Phys. **29**, 108 (1999); cond-mat/9905064.
3. A. I. Olemskoĭ, Pis'ma Zh. Éksp. Teor. Fiz. **69**, 391 (1999) [JETP Lett. **69**, 423 (1999)].
4. K. V. Chukbar, Zh. Éksp. Teor. Fiz. **108**, 1875 (1995) [JETP **81**, 1025 (1995)].
5. R. Rammal, G. Toulouse, and M. A. Virasoro, Rev. Mod. Phys. **58**, 765 (1986).
6. A. I. Olemskoĭ, *Fractals in Condensed Matter Physics*, in Physics Reviews, Ed. by I. M. Khalatnikov (Gordon and Breach, London, 1996), Vol. 18, Part 1.
7. A. I. Olemskoĭ and A. D. Kiselev, Phys. Lett. A **247**, 221 (1998).
8. E. M. Lifshitz and L. P. Pitaevskiĭ, *Physical Kinetics* (Nauka, Moscow, 1979; Pergamon Press, Oxford, 1981).
9. C. Tsallis, in *Nonextensive Statistical Mechanics and Its Applications*, Lecture Notes in Physics, Ed. by S. Abe and Y. Okamoto (Springer-Verlag, Berlin, 2000).
10. A. I. Olemskoĭ, Usp. Fiz. Nauk **168**, 287 (1998) [Phys. Usp. **41**, 269 (1998)].

Translated by R. Tyapaev

JETP Letters, Vol. 71, No. 7, 2000, pp. 289–292. Translated from Pis'ma v Zhurnal Éksperimental'noĭ i Teoreticheskoĭ Fiziki, Vol. 71, No. 7, 2000, pp. 418–423.

CONDENSED MATTER

Temperature Dependence of the Energy Gap in Bi2223 Metal Oxide Superconductor

V. M. Svistunov, V. Yu. Tarenkov*, A. I. D'yachenko*, and E. Hatta****

** Galkin Physicotechnical Institute, National Academy of Sciences of Ukraine, Donetsk, 340114 Ukraine*

*** Nanoelectronics Laboratory, Faculty of Engineering, Hokkaido University, Sapporo 060, Japan*

Received February 24, 2000

Spectroscopic studies of the silver–optimum-doped Bi2223 contacts show that the temperature dependence of the parameter Δ follows the BCS curve. However, the tunnel measurements performed for the same series of specimens did not reveal any temperature dependence of the energy gap Δ. The feature observed in the tunnel density of states was retained at temperatures $T > T_c$, manifesting the presence of the temperature-independent pseudogap E_p. The difference between the data obtained with tunnel spectroscopy and Andreev reflection spectroscopy is explained by the fact that the latter measures the true superconducting energy gap $\Delta_s(T)$, whereas the peaks of the tunneling conductivity are related to the total energy gap Δ of cuprates, which includes both the parameter Δ_s and the pseudogap E_p: $\Delta \approx \sqrt{\Delta_s^2 + E_p^2}$. © *2000 MAIK "Nauka/Interperiodica".*

PACS numbers: 74.20.-z; 74.50.+r

One of the most interesting properties of metal oxide superconductors is the possibility of the formation of a gaplike structure at $eV = E_p$ in the spectrum of the normal excitations of cuprates [1–6]. The absence of a universally accepted theoretical model of the pseudogap E_p [1, 7, 8], as well as the possibility of an ambiguous interpretation of the optical [1, 6] and photoemission data [1, 3–5], call for new experiments that would clarify the relationship between E_p and the superconducting energy gap Δ_s in cuprates. For such experimental studies, contact spectroscopic methods (tunnel spectroscopy and Andreev reflection spectroscopy) offer considerable promise.

Tunneling spectroscopy is sensitive to any gap in the spectrum of quasiparticle excitations [9], whereas Andreev reflection [10] occurs only at the superconducting energy gap Δ_s. This fact stimulated our studies with tunneling and Andreev contacts made on identical Bi2223 cuprate specimens. The tunnel measurements revealed no temperature dependence of the Δ gap for $T \longrightarrow T_c$. Above T_c, the "tunnel" gap Δ was spread over a wide region, which can be interpreted as a manifestation of the pseudogap E_p [11]. At the same time, the Andreev contact measurements showed that the energy gap $\Delta_s(T)$ of cuprates exhibits a temperature dependence close to the BCS curve. The difference in the temperature behavior of the tunnel and Andreev spectra allows certain conclusions to be drawn about the Fermi surface topology and the pseudogap anisotropy in cuprate superconductors.

The experiments were performed on both optimum-doped and underdoped Bi2223 cuprate specimens. To prepare tunneling and Andreev contacts of the "break junction" type, highly textured ceramic plates were used [12]. The initial ceramics (95% of the $Bi_{1.6}Pb_{0.4}Sr_{1.8}Ca_{2.2}Cu_3O_x$ phase, $T_c \approx 113$ K) was obtained by solid-phase synthesis from chemically pure oxides. In one experimental cycle, ten plates of dimensions $1 \times 0.1 \times 12$ mm were fabricated with silver current and voltage leads sealed in. To obtain oxygen-deficient specimens, half of the plates were heated in an oven to a temperature of 845°C and held at this temperature for two hours. Then the plates were rapidly (within ±3 min) cooled to room temperature. As a result of such quenching, the resistance of the specimens increased and the critical temperature decreased to $T_c \approx$ 107 K, while the transition curve was shifted parallel to the $R(T)$ dependence for the optimum-doped metal oxide.

To obtain a contact of the break junction type, a plate lying on a flexible steel substrate was covered with lacquer. Then the substrate was bent until a microcrack was formed in the ceramics, which was monitored by the change in the specimen's resistance. Depending on the uncontrolled factors, either an SIS tunneling microcontact ($r_n \sim$ 50–100 Ω) or an SNS Andreev microcontact ($r_n \sim$ 1–5 Ω) was formed. Here, S, N, and I denote the superconductor, the normal constriction, and the insulator, respectively. For high bias voltages V, a metallic conductivity was observed for the Andreev contacts, whereas the conductivity of the SIS

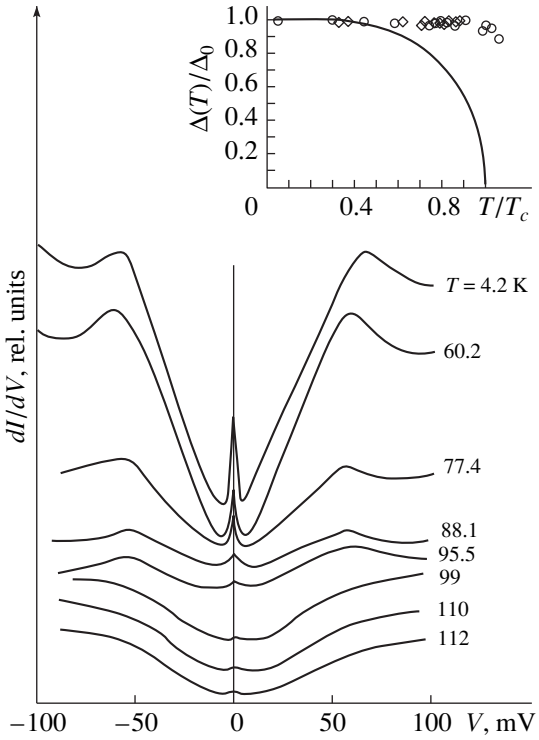

Fig. 1. Conductivity of a Bi2223–insulator–Bi2223 tunneling contact at different temperatures. The inset shows the $\Delta(T)$ dependence obtained for the specimen under study and the BCS curve.

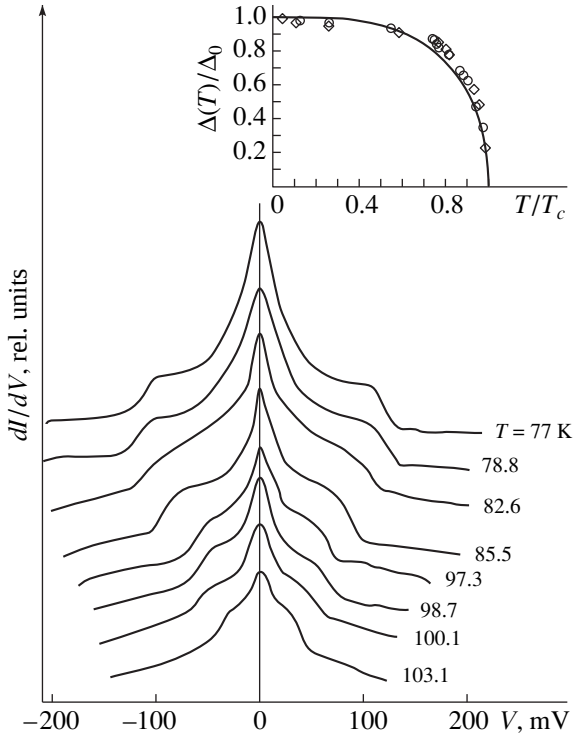

Fig. 2. Andreev reflection spectrum displaying the superconducting energy gap Δ_s for Bi2223 cuprate at different temperatures. The inset shows the temperature dependence of Δ_s and the BCS dependence.

contacts exhibited a parabolic behavior typical of electron tunneling.

Figure 1 presents the conductivity of a symmetric SIS contact of the break junction type at different temperatures. At a low bias voltage $V = 5$ mV, the resistance of the tunneling contact rapidly increased with decreasing temperature below the critical temperature T_c of the cuprate, indicating the opening of the energy gap Δ_s. The critical temperature T_c of metal oxide was determined from the center of its transition curve $R(T)$. The ratio of the resistances $r(V)$ of the tunneling contact at $eV = eV_0 \ll \Delta$ and $eV > \Delta$ in the temperature range $T \sim$ 4.2–20 K was typical of tunneling contacts: $r(V_0)/r(V > \Delta) \sim 10^2$. The characteristic feature of all tunneling contacts was a sharp conductivity peak at zero bias voltage because of the *d*-symmetry of the order parameter of the superconductor under study. As in [12], the value of 4Δ in SIS contacts was taken to be equal to the distance between the maxima in the dI/dV curves.

From the tunneling spectra shown in Fig. 1, it is difficult to make any inferences about the temperature dependence $\Delta(T)$ (inset in Fig. 1). According to Fig. 1, the $r(V_0)/r(V > \Delta)$ ratio only decreased with increasing temperature. The gap characteristics of both optimum-doped (T_c = 131 K) and underdoped (T_c = 107 K) cuprates showed the same behavior.

A qualitatively different temperature dependence of the energy gap was observed for the SNS contacts that unambiguously exhibited Andreev reflection. Figure 2 shows the characteristics of such a contact recorded at different temperatures. One can see that the steplike feature observed in the conductivity at the voltage V_c and corresponding to the $2\Delta_s(T)$ value is markedly shifted toward lower energies at $T \longrightarrow T_c$. The inset in Fig. 2 shows the $\Delta_s(T)$ values for different SNS contacts. According to these data, the temperature curve observed for the energy gap $\Delta_s(T)$ in the Andreev contacts is similar to the BCS curve.

Thus, the $\Delta_s(T)$ and $\Delta(T)$ dependences obtained by different spectroscopic methods contradict each other (Figs. 1, 2). This discrepancy is primarily caused by the fact that Andreev reflection occurs only at the superconducting energy gap $\Delta_s(T)$. In the contacts with a direct metallic conductivity, the reflection of charge carriers from the pseudogap has a quasiparticle character. In this case, there is no transformation from the electronlike state to the holelike state, for which a condensate of Cooper pairs is necessary. The condensate does not participate in the reflection from the pseudogap, the reflection not being specular because of the fluctuational character of the pseudogap. As a result, the reflection from the pseudogap contributes to the ordinary "normal" electron reflection, which is

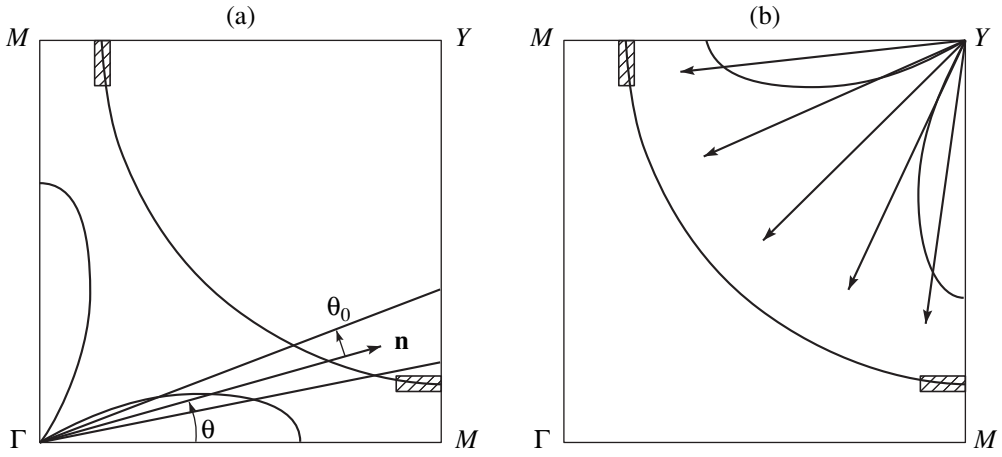

Fig. 3. (a) Schematic diagram illustrating the tunneling directivity toward a portion of the Fermi surface of metal oxide. The contact plane is perpendicular to the basal plane of cuprate. The hatched areas correspond to the "hot spots" of the Fermi surface. The Fermi surface is centered at the point *Y* of the Brillouin zone. The butterfly of the $d_{x^2-y^2}$ order parameter is centered at the point Γ. (b) Isotropic structure of Andreev reflection that allows one to detect the energy gap for all parts of the Fermi surface.

accompanied by a considerable shortening of the quasiparticle lifetime (the Dynes parameter Γ increases).

Hence, each of the contact methods considered above yields objective information on the excitation spectrum of the superconductor, but this information is "collected" from different areas of the Brillouin zone. Figure 3 schematically represents a quarter of the Brillouin zone of Bi2223 with a portion of the Fermi surface of metal oxide and the $\Delta(\mathbf{k})$ dependence (on the assumption of $d_x2_{-y}2$ wave pairing). The hatched areas represent the Fermi surface domains in the vicinity of which the Van Hove singularity [1] is observed and the pseudogap [2–4] manifests itself. The angle between the normal to the tunneling contact plane and the crystallographic *a*-axis in the *ab* plane is denoted by θ. As a rule, the θ angle is small (i.e., the fracture plane of a Bi2223 microcrystal is normal to the *a*- or *b*-axis). The tunneling occurs at angles within a narrow cone with cone angle $\theta_0 < 10°$ because of the increase in the effective barrier thickness at large θ angles [9]. Therefore, the gap characteristic of homogeneous tunneling contacts can be observed at the θ angles for which at least the edge of the Fermi surface falls within the tunneling cone $|\theta| < \theta_0$ (Fig. 3a). In such a situation, one should observe a gap $\Delta(\varphi)$ that is smaller than the maximal possible value Δ_0: $\Delta(\varphi) = \Delta_0\cos(2\varphi)$.

The Δ_0 value can be reflected only in the characteristics of the Andreev contact, provided that this is not prevented by a short electron lifetime in the "hot spot" regions (Fig. 3b) where the pseudogap E_p reaches its maximum [1, 6]. In reality, for the optimum-doped specimens (when the pseudogap effect is weaker [4–6]), the value of Δ (Bi2223) observed in the Andreev contacts was 52–55 meV, whereas for the tunneling contacts, the value of $\Delta(\varphi)$ did not exceed 40–44 meV.

Andreev reflection has no limitations in the angle θ, and the direction of electron motion is determined by the electron group velocity (Fig. 3b). In this case, all parts of the Fermi surface in the k_x, k_y plane are available for observation, and the energy gap can be measured for all directions θ. The presence of a clearly defined edge of the Fermi surface, at least at some angular interval in the k_x, k_y plane, is the condition for the observation of the superconducting energy gap $\Delta(\mathbf{k})$ in the Andreev contacts. Therefore, the appearance of a sharp step in the characteristics of the Andreev contacts (Fig. 2) testifies that the Bi2223 phase (with different degrees of doping) has Fermi surface areas that are not "spoiled" by the presence of the pseudogap and are characterized by a temperature dependence $\Delta_s(T)$ close to the BCS curve. In other words, the quasiparticle lifetime in these areas is sufficiently long, so that the Fermi-liquid analysis is applicable.

The situation is very different for the tunneling contact. Because of the narrow directivity of the tunneling effect, the tunneling cone more often includes the "hot" areas of the Fermi surface (Fig. 3a, $\theta < 20°$), where the pseudogap E_p manifests itself. As is known [1, 6], the pseudogap weakly depends on temperature and, in addition, the value of E_p far exceeds Δ_s in an underdoped region [2, 7, 11]. This hinders the observation of the temperature dependence of the effective energy gap $\Delta \approx \sqrt{\Delta_s^2 + E_p^2}$.

In closing, note that the observation of a sharp energy-gap edge in the Andreev contacts of metal oxides (with different degrees of doping) points to the possibility of applying the Fermi-liquid description to a major part of the Fermi surface of cuprates (near the diagonals of the Brillouin zone). In this region, the temperature dependence of the energy gap can be described

in terms of the mean-field approximation. However, such an approach is unacceptable in the vicinity of the *M* points of the Brillouin zone, where the pseudogap, i.e., the energy gap in the spectrum of normal excitations, comes into play.

Today, the most advanced model of high-temperature superconductors, which includes the stripe structures and the pseudogap, is the Emery–Kivelson model of the antiferromagnetic proximity effect [13]. In this model, the superconducting energy gap and the pseudogap coincide at $T < T_c$, which does not agree with our experimental results.

We are grateful to Prof. K. Mukasa, M. Oda, and Prof. M. Ido for useful discussions. V.M. Svistunov acknowledges the support provided to him by the Ministry of Education, Science, and Culture of Japan during his stay at Hokkaido University.

REFERENCES

1. Z.-X. Shen and D. S. Dessau, Phys. Rep. **253**, 1 (1995).
2. A. G. Loeser, Z.-X. Shen, D. S. Dessau, *et al.*, Science (Washington, D.C.) **273**, 281 (1996).
3. J. M. Harris, A. G. Loser, D. S. Marshall, *et al.*, Phys. Rev. B **54**, R15665 (1996).
4. D. S. Marshall, D. S. Dessau, A. G. Loeser, *et al.*, Phys. Rev. Lett. **76**, 4841 (1996).
5. M. R. Norman, H. Ding, H. Fretwell, *et al.*, Phys. Rev. B **60**, 7585 (1999); M. R. Norman, H. Ding, M. Randeria, *et al.*, Nature (London) **392**, 157 (1998); N. L. Saini, J. Avila, A. Bianconi, *et al.*, Phys. Rev. Lett. **79**, 3467 (1997).
6. J. Demsar, B. Podobnik, V. V. Kabanov, *et al.*, Phys. Rev. Lett. **82**, 4918 (1999); D. Mihailovic, T. Mertelj, and K. A. Müller, Phys. Rev. B **57**, 6116 (1998).
7. V. J. Emery and S. A. Kivelson, cond-mat/9902179 (1999); M. R. Norman, M. Randeria, H. Ding, and J. C. Campuzano, Phys. Rev. B **57**, R11093 (1998); O. Tchernyshov, Phys. Rev. B **56**, 3372 (1997).
8. J. W. Loram, K. A. Mirza, J. R. Cooper, and J. L. Tallon, Physica C (Amsterdam) **282–287**, 1405 (1997); J. Bok and J. Bouvier, Physica C (Amsterdam) **274**, 1 (1997).
9. E. L. Wolf, *Principles of Electron Tunneling Spectroscopy* (Oxford Univ. Press, New York, 1985; Naukova Dumka, Kiev, 1990).
10. A. F. Andreev, Zh. Éksp. Teor. Fiz. **46**, 1823 (1964) [Sov. Phys. JETP **19**, 1228 (1964)].
11. Ch. Renner, B. Revaz, J.-Y. Genoud, *et al.*, Phys. Rev. Lett. **80**, 149 (1998); T. Ekino, Y. Sezaki, and H. Fujii, Phys. Rev. B **60**, 6916 (1999); D. Mihailovic, V. V. Kabanov, K. Zagar, and J. Demsar, Phys. Rev. B **60**, R6995 (1999).
12. V. M. Svistunov, V. Yu. Tarenkov, A. I. D'yachenko, and R. Aoki, Fiz. Tverd. Tela (St. Petersburg) **39**, 1764 (1997) [Phys. Solid State **39**, 1572 (1997)].
13. V. J. Emery, S. A. Kivelson, and J. M. Tranquada, Proc. Natl. Acad. Sci. USA **96**, 8814 (1999); Phys. Rev. B **59**, 14712 (1999).

Translated by E. Golyamina

JETP Letters, Vol. 71, No. 7, 2000, pp. 293–297. From Pis'ma v Zhurnal Éksperimental'noĭ i Teoreticheskoĭ Fiziki, Vol. 71, No. 7, 2000, pp. 424–429.

CONDENSED MATTER

Martensitic Transition in Single-Crystalline α-GeO_2 at Compression[1]

V. V. Brazhkin, E. V. Tat'yanin, A. G. Lyapin, S. V. Popova, O. B. Tsiok, and D. V. Balitskiĭ*

Institute of High-Pressure Physics, Russian Academy of Sciences, Troitsk, Moscow region, 142092 Russia

** Moscow State University, Vorob'evy gory, Moscow, 119899 Russia*

Received February 28, 2000

We present a structural study of single crystalline quartz-like α-GeO_2 compressed to pressures up to 12 GPa and subsequently quenched to ambient conditions. The transition to a new crystalline phase with a distorted rutile structure, occurring in the pressure interval 8 to 12 GPa, was established. The structure of the new phase was identified from X-ray and electron diffraction data as $P2_1/c$ monoclinic. Electron transmission and scanning microscopy provide direct evidence of the martensitic (or displacive) nature of the transition, indicating, in particular, the lamellar morphology and crystallographic orientation relation between the initial α-quartz and final new monoclinic phases. Upon heating, the new monoclinic phase transforms to the rutile-type structure with a similar (and similarly oriented) oxygen structure motif. Finally, we discuss the difference in high-pressure behavior of single-crystalline and polycrystalline samples transforming to the new crystalline and amorphous phases, respectively. *© 2000 MAIK "Nauka/Interperiodica".*

PACS numbers: 61.50.Ks; 81.30.Kf; 81.40.Vw; 64.70.Kb

Polymorphism of silica SiO_2 is of great interest for geophysics, earth and planetary sciences, and glass technology. Germanium dioxide GeO_2 is the closest structural and polymorphic analogue of silica. In particular, the α-quartz modification of GeO_2 is structurally very similar to α-quartz SiO_2 under pressure (they have a close intertetrahedral angle) [1]. From this point of view, the study of GeO_2 under pressure could extend our knowledge about tetrahedrally networked crystalline and glassy compounds, including silicates and germanates.

α-Quartz SiO_2 undergoes gradual pressure-induced amorphization from 15 to 30 GPa with an intermediate crystalline-to-crystalline transition (quartz I–II) at 21 GPa [2–4]. Amorphous silica samples quenched to normal conditions display unusual properties, such as anisotropy and "memory" effects [5], that may be described theoretically [6]. In nonhydrostatic conditions, α-quartz transforms to a mixture of amorphous and new crystalline phases [7], probably based on the edge-sharing SiO_6-octahedra structures. Another low-pressure polymorph of silica, cristobalite, transforms to a stishovite-like phase under quasi-hydrostatic compression [8]. A variety of theoretically proposed silica structures with highly coordinated Si atoms (Z > 4) [9–12] suggests a complicated picture of metastable high-pressure polymorphism in silica.

The α-GeO_2 phase transforms in the pressure interval 6–8 GPa to the amorphous state with a rutile-like short-range order structure, the coordination of Ge atoms being changed from four- to sixfold at high pressure [13–17]. The low pressure of amorphization for germania glass gives the opportunity to study large samples under pressure. Another motivation for this work is to study the influence of sample morphology and nonhydrostaticity on the transformation type. There are indications that the type of high-pressure transformation in $AlPO_4$ can depend on the initial crystal size [18]. Unfortunately, the α-quartz modification of GeO_2 is metastable under normal conditions [19], and only polycrystalline specimens with a small grain size have been used for high-pressure investigations to date. Here, we present the structural study of a sample recovered at normal conditions after both hydrostatic and quasi-hydrostatic compression of large single crystals of α-GeO_2. This type of study is of special interest for understanding more general aspects of the solid state amorphization phenomenon [20–22].

Experimental. Large α-GeO_2 single crystals (several millimeters in size) were prepared using a novel hydrothermal technique described in detail in [23, 24]. The pieces used in our experiments were $4 \times 4 \times 1$ mm platelets with the crystallographic *c*-axis perpendicular to the largest sides. The high structural quality of α-GeO_2 single crystals earlier allowed us to study the elastic constants of quartz-like GeO_2 by Brillouin spectroscopy [25].

High pressure up to 12 GPa was generated in the toroid-type chamber [26] with a 4 : 1 methanol–ethanol mixture and polycrystalline NaCl as the hydrostatic or quasihydrostatic pressure transmitting media, respectively. The compression and subsequent decompression of samples were carried out at room temperature with

[1] This article was submitted by the authors in English.

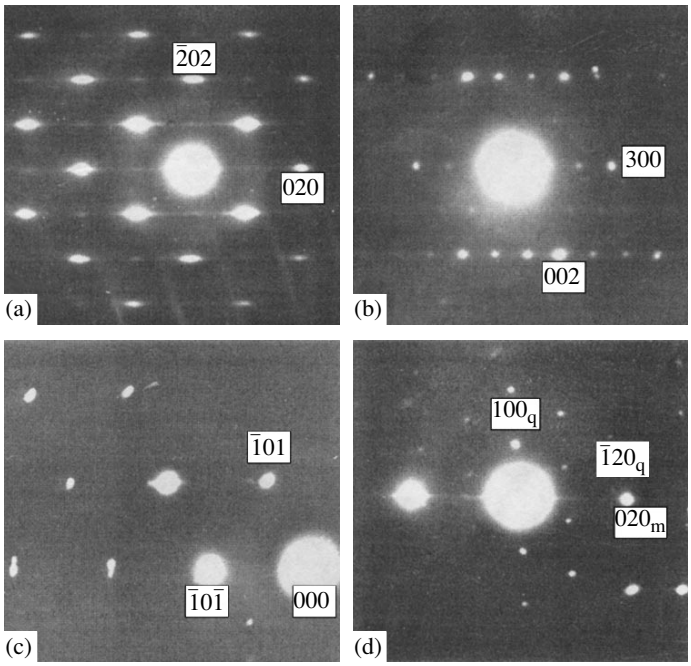

Fig. 1. Electron diffraction patterns: (a, b) from the monoclinic phase of GeO_2 for 101 and 010 zones (reciprocal lattice planes), respectively; (c) from the rutile phase (010 zone of rutile structure) obtained upon annealing of the monoclinic phase; and (d) from the partly transformed area revealing both initial α-quartz (001 zone) and new monoclinic modifications (the reflections for $\bar{1}07$ and 001 zones can be observed) related transitionally and crystallographically to one another (reflections of the monoclinic phase are marked by index "m"). The patterns b and c are obtained from the same crystallite before and after annealing, respectively.

the pressure change rate of ~0.2 GPa/min. The structure of the recovered samples was studied by both electron (a JEM-100C transmission electron microscope, TEM) and X-ray (the Debye–Sherer method) diffraction techniques. The morphology of the samples was studied by electron scanning microscopy (Leica S430 and Stereoscan MK-2). The density of the samples was measured by the picnometric method. The MOM-C Derivatograph (Hungary) was used for the annealing of samples at ambient pressure.

Results and discussion. In our experiments, we applied pressure to both polycrystalline (with small grain size on the order of a micron or less) and single-crystalline α-GeO_2 samples. The polycrystalline samples recovered from pressures higher than 8 GPa were completely disordered, in accordance with the published data on the pressure-induced amorphization of α-GeO_2. Quite a different picture was revealed for single-crystalline α-GeO_2. A transition to a new crystalline GeO_2 polymorph takes place instead of to an amorphous phase. The transition occurs in a wide pressure range starting at 7 to 7.5 GPa and finishing at 11.5 to 12 GPa. At intermediate pressures, we observed a mixture of the new high-pressure phase and the initial quartz-like polymorph. The transition was found to follow almost identical scenarios under both hydrostatic and quasi-hydrostatic conditions.

X-ray diffraction data revealed that the new high-pressure GeO_2 phase had a structure fairly similar to that of rutile-type GeO_2, but with a more complicated X-ray diffraction pattern (see table). In particular, strong reflections of the new phase with the *d*-space of 0.240, 0.218, and 0.210 nm coincide with, or are very close to, the (101), (200), and (111) rutile reflections, respectively. On the other hand, the strong reflections with *d*-spacing of 0.290, 0.261, and 0.230 nm are absent in the diffraction pattern of the rutile phase.

Electron diffraction on a single crystallite of the recovered material provides more comprehensive structural data (table and Fig. 1). Among the known and theoretically proposed GeO_2 (SiO_2) structures, the 3×2 monoclinic structure with the $P2_1/c$ space group [11] was established to agree best with the diffraction from the new phase (see table). This structure consists of 3×2 kinked edge-sharing GeO_6 octahedral chains and can be regarded as a distorted hexagonal close-packed (hcp) array of oxygen ions with one-half of the available octahedral interstices occupied by Ge ions in a specific zigzag (3×2) order [11]. The indexing of diffraction patterns in accordance with this consideration leads to the following lattice parameters: $a = 0.815$ nm, $b = 0.436$ nm, $c = 0.535$ nm, $\alpha = \gamma = 90°$, and $\beta = 118°$.

The new phase annealing at normal pressure displayed its metastability, since it gradually transformed to rutile GeO_2 in the temperature interval from 200 to 500°C with a small exothermal effect. When the new phase transforms to the stable rutile modification during annealing, the reflection $d = 0.240$ nm from the cor-

Experimental *d*-spacing and relative intensities (only for X-ray data) for the new GeO_2 phase, compared with the *d*-spacing of the GeO_2 rutile and 3×2 monoclinic $P2_1/c$ structures

New phase			Rutile*		$P2_1/c$-type**			
TEM	X-ray							
d (nm)	d (nm)	I/I_{max} (%)	hkl	d_{hkl} (nm)	h	k	l	d_{hkl} (nm)
0.473								
0.387	0.393	5						
0.335	0.336	20			1	1	$\bar{1}$	0.335
0.321					0	1	1	0.320
	0.312	10	110	0.311				
0.289	0.290	80			2	1	$\bar{1}$	0.289
0.264					1	0	$\bar{2}$	0.264
0.263					1	1	1	0.263
0.262	0.261	60			2	0	$\bar{2}$	0.262
0.240	0.240	100	101	0.240	3	0	0	0.240
0.236	0.235	40			0	0	2	0.236
0.231	0.230	50			3	0	$\bar{2}$	0.231
					3	1	$\bar{1}$	0.230
0.218	0.218	30	200	0.220	0	2	0	0.218
0.210	0.210	30	111	0.210	3	1	0	0.210
					2	1	1	0.209
0.208	0.207	20			0	1	2	0.208
0.199					1	0	2	0.199
			210	0.197				
0.193					4	0	$\bar{2}$	0.193
0.168	0.168	10			1	2	$\bar{2}$	0.168
					2	2	$\bar{2}$	0.168
0.165	0.164	15			2	0	2	0.165
			211	0.162				
0.161					3	2	0	0.161
					5	0	$\bar{2}$	0.161
					0	2	2	0.160
0.159	0.159	80			3	2	$\bar{2}$	0.159
			220	0.155				
0.150	0.151	10			5	1	$\bar{1}$	0.150
			002	0.143				
0.139	0.138	40			4	1	1	0.139
					3	0	2	0.139
0.136	0.135	10			6	0	$\bar{2}$	0.136

Notes: * Lattice parameters are $a = 0.4396$ nm and $c = 0.2863$ nm.

** Lattice parameters are $a = 0.815$ nm, $b = 0.436$ nm, $c = 0.535$ nm, $\alpha = \gamma = 90°$, and $\beta = 118°$.

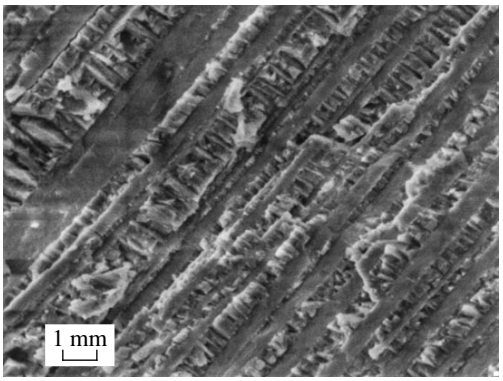

Fig. 2

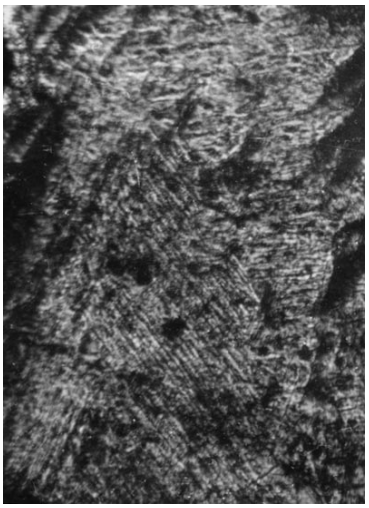

Fig. 3

responding part of the sample is the same before and after the transition (Figs. 1b, 1c). This reflection corresponds to the (101) rutile lattice planes. The transition of the 3×2 monoclinic structure to the rutile one may be interpreted as a reordering of Ge ions in the distorted hcp oxygen array, when the oxygen structural motif is retained. The atomic packings of the (101) planes of the rutile structure and the (100) planes of the new phase are similar in this case. The crystallographic density of the 3×2 monoclinic phase (6.22 g/cm^3) is slightly lower than that of the rutile GeO_2 (6.28 g/cm^3); the experimentally measured value is (6.1 ± 0.05 g/cm^3).

Electron diffraction from the areas containing both initial α-quartz and the final new phase in the incompletely transformed samples (Fig. 1d) provides direct evidence of the martensitic (or displacive) mechanism of the pressure-induced crystalline–crystalline transition in α-GeO_2. The lamellar morphology of the recovered samples, visualized by scanning electron microscopy, also proves this conclusion. We have established the following crystallographic orientational relations between the initial quartz-like and new phases, if the latter is identified as the 3×2 monoclinic $P2_1/c$ structure: $(100)^{\alpha-quartz}$ nearly $\parallel$ $(100)^{monoclinic}$ and $(\bar{1}20)^{\alpha-quartz}$ nearly $\parallel (010)^{monoclinic}$. There are three possible orientations for the produced phase with respect to the initial α-GeO_2 crystal, because α-quartz has three planes equivalent to the (100). The surface morphology pictures observed for the recovered samples support this statement, the three lamellar sets being relatively located at an angle of 60° to each other.

More careful examination of the experimental data showed that the agreement between experimental data and the new-phase identification as a 3×2 monoclinic structure was still not ideal. First, in the experimental diffraction spectra (table), there are some reflections forbidden for the $P2_1/c$ structure; second, there is no good agreement between the experimental and the calculated reflection intensities (this point is not considered in detail here). These observations indicate that the new GeO_2 phase, probably based on the 3×2 monoclinic structure, contains large amounts of the (010) packing defects of the monoclinic lattice.

The mechanism of pressure-induced crystalline–crystalline transition demands a special discussion. The crystallographic relation, as well as the specifically oriented lamellar morphology provide unambiguous evidence of the atomic-cooperative displacive transformation mode. Clearly, the transition must be governed in this case by dynamic softening principles. The observation of a highly coordinated SiO_2 phase (obtained under nonhydrostatic compression) with a structure fairly similar to the 3×2 monoclinic phase [7, 11] indicates that the transition to such a structure is an ordinary phenomenon for the tetrahedrally networked α-quartz structure type. The hydrostaticity degree of the high-pressure environment is an important dynamic factor affecting the phonon spectrum and, hence, the transition mode. In contrast to SiO_2, the distorted rutile structure of GeO_2 was obtained in both hydrostatic and quasi-hydrostatic conditions. The difference in the SiO_2 and GeO_2 behaviors should be associated with specific features of the lattice dynamics and the corresponding phonon spectra under pressure. One should note that dynamic softening principles are now used for understanding solid-state amorphization [21, 22], and the softening of open-packed structures (in particular, tetrahedrally coordinated ones) seems to be quite a general phenomenon [22].

The α-quartz-to-rutile transition in SiO_2 and GeO_2 occurring under pressure at high temperatures is governed by the diffusion reconstruction. At room and lower temperatures, when diffusion becomes retarded, the softening of the particular modes in the phonon spectrum becomes a driving force triggering structural reconstruction. This gives a key for understanding the difference between the crystalline-to-crystalline, crystalline-to-amorphous, and amorphous-to-amorphous

transformations in quartz-like GeO_2. The coordination transformation in amorphous GeO_2 under pressure [14, 15, 27, 28] is determined by a wide spectrum of activation energies for local coordination reconstructions [28], the property which seems to be inherent in the disordered GeO_2 network because of the dispersion of bond lengths and bond–bond angles, as well as the topological disorder in the arrangement of GeO_4 tetrahedra. In the opposite case of single-crystalline α-GeO_2, the transition results in a coherent cooperative atomic motion. Polycrystalline α-GeO_2 is an intermediate case. When the average grain size is small enough, the scenario of coherent displacive transition is destroyed, because the dispersion of stresses in individual crystallites and a large portion of defective atomic sites at grain boundaries cause the disorder. These factors seem to create a great variety of topologically different displacive soft modes for coordination reconstruction and lead to the formation of the topologically disordered GeO_2 structure, although the different displacive modes may have rather similar geometrical reasons for softening (e.g., like twisting of SiO_4 tetrahedra in the α-quartz near the pressure of amorphization transformation [29]). One should note that in the amorphous samples thus obtained the structural disorder varies from really amorphous nanoregions to those with a high degree of rutile-type crystallinity [14]. The difference between the pressure intervals for solid state amorphization and the crystalline-to-crystalline transition in materials with the same atomic structure but different morphology emphasizes the dynamic difference in the paths of transformation. The properties of high-pressure amorphous samples obtained from starting amorphous and polycrystalline quartz-like GeO_2 are also different [13, 14].

Further structural and dynamic investigations of single α-GeO_2 crystals under pressure, including Raman and Brillouin spectroscopy studies, are expected to provide additional understanding of the high-pressure behavior of tetrahedrally networked GeO_2 and SiO_2 polymorphs. Computer simulation will be very suitable for the identification of real displacive modes during the transition.

We are grateful to S.C. Bayliss, A.V. Sapelkin, M. Grimsditch, and A. Polian for stimulating discussions; to I. Fletcher (Faculty of Applied Science, De Montfort University, Leicester, LE1 9BH, England) for assistance in the scanning microscopy study; and to N.F. Borovikov and L.A. Ivanov for assistance in the optical microscopy study. This work was supported in part by the Russian Foundation for Basic Research (project no. 98-02-16325) and by the program "Integratsiya" (grant no. 250).

REFERENCES

1. L. Levien, C. T. Prewitt, and D. J. Weidner, Am. Mineral. **65**, 920 (1980).
2. R. J. Hemley, A. P. Jephcoat, H.-K. Mao, *et al.*, Nature (London) **334**, 52 (1988).
3. K. J. Kingma, C. Meade, R. J. Hemley, *et al.*, Science (Washington, D.C.) **259**, 666 (1993).
4. K. J. Kingma, R. J. Hemley, H.-K. Mao, and D. R. Veblen, Phys. Rev. Lett. **70**, 3927 (1993).
5. L. E. McNeil and M. Grimsditch, Phys. Rev. Lett. **68**, 83 (1992).
6. J. S. Tse and D. D. Klug, Phys. Rev. Lett. **70**, 174 (1993).
7. K. J. Kingma, H.-K. Mao, and R. J. Hemley, High-Pressure Res. **14**, 363 (1996).
8. M. Yamakata and T. Yagi, Rev. High-Pressure Sci. Technol. **7**, 107 (1998).
9. B. B. Karki, M. C. Warren, L. Stixrude, *et al.*, Phys. Rev. B **55**, 3465 (1997).
10. J. Badro, D. M. Teter, R. T. Downs, *et al.*, Phys. Rev. B **56**, 5797 (1997).
11. D. M. Teter, R. J. Hemley, G. Kresse, and J. Hafner, Phys. Rev. Lett. **80**, 2145 (1998).
12. R. M. Wentzcovitch, C. D. Silva, J. R. Chelikowsky, and N. Binggeli, Phys. Rev. Lett. **80**, 2149 (1998).
13. T. Yamanaka, T. Shibata, S. Kawasaki, and S. Kume, in *High-Pressure Research: Application to Earth and Planetary Sciences*, Ed. by Y. Syono and H. Manghnani (American Geophysical Union, Washington, D.C., 1992), p. 493.
14. G. H. Wolf, S. Wang, C. A. Herbst, *et al.*, in *High-Pressure Research: Application to Earth and Planetary Sciences*, Ed. by Y. Syono and H. Manghnani (American Geophysical Union, Washington, D.C., 1992), p. 503.
15. J. P. Itie, A. Polian, G. Calas, *et al.*, Phys. Rev. Lett. **63**, 398 (1989).
16. N. Suresh, G. Jyoti, S. C. Gupta, *et al.*, J. Appl. Phys. **76**, 1530 (1994).
17. S. Kawasaki, J. Mater. Sci. Lett. **15**, 1860 (1996).
18. P. Gillet, J. Badro, B. Varrel, and P. F. McMillan, Phys. Rev. B **51**, 11262 (1995).
19. E. Yu. Tonkov, *High Pressure Phase Transformations*: A Handbook 1-2 (Gordon & Breach, Philadelphia, 1992).
20. E. G. Ponyatovsky and O. I. Barcalov, Mater. Sci. Rep. **8**, 1471 (1992).
21. V. V. Brazhkin and A. G. Lyapin, High-Pressure Res. **15**, 9 (1996).
22. A. G. Lyapin and V. V. Brazhkin, Phys. Rev. B **54**, 12036 (1996).
23. D. V. Balitskiĭ, Y. Pushchanskiĭ, and V. S. Imlitsky, in *Abstracts of the 11th International Conference on Crystal Growth, The Hague, 1995*, p. 573.
24. V. S. Balitskiĭ, D. V. Balitskiĭ, D. Yu. Putsharovskiĭ, *et al.*, in *Experimental and Theoretical Modeling of the Processes of Mineral Formation*, Ed. by V. A. Zharikov and V. V. Fed'kin (Nauka, Moscow, 1998), p. 498.
25. M. Grimsditch, A. Polian, V. Brazhkin, and D. Balitskiĭ, J. Appl. Phys. **83**, 3018 (1998).
26. L. G. Khvostantsev, L. F. Vereshchagin, and A. P. Novikov, High Temp.–High Pressures **9**, 637 (1977).
27. K. H. Smith, E. Shero, A. Chizmeshya, and G. H. Wolf, J. Chem. Phys. **102**, 6851 (1995).
28. O. B. Tsiok, V. V. Brazhkin, A. G. Lyapin, and L. G. Khvostantsev, Phys. Rev. Lett. **80**, 999 (1998).
29. S. V. Goryaĭnov and N. N. Ovsyuk, Pis'ma Zh. Éksp. Teor. Fiz. **69**, 431 (1999) [JETP Lett. **69**, 467 (1999)].

JETP Letters, Vol. 71, No. 7, 2000, pp. 298–302. Translated from Pis'ma v Zhurnal Éksperimental'noĭ i Teoreticheskoĭ Fiziki, Vol. 71, No. 7, 2000, pp. 430–436.

CONDENSED MATTER

Observation of Coherent Phonon States in Porous Silicon Films

A. L. Dobryakov*, V. A. Karavanskiĭ, S. A. Kovalenko***, S. P. Merkulova*, and Yu. E. Lozovik***

**Institute of Spectroscopy, Russian Academy of Sciences, Troitsk, Moscow region, 142092 Russia*
***Institute of General Physics, Russian Academy of Sciences, ul. Vavilova 38, Moscow, 117942 Russia*
**** Humboldt Universität Berlin, D-10117 Berlin, Germany*
e-mail: lozovik@isan.troitsk.ru

Received March 6, 2000

The dynamics of differential transmission and reflectance spectra of porous silicon films was studied using the femtosecond excitation technique ($\tau \approx 50$ fs, $\hbar\omega_{pump} = 2.34$ eV) with supercontinuum probing ($\hbar\omega_{probe} = 1.6$–$3.2$ eV) and controlled time delay with a step of $\Delta t = 7$ fs between the pump and probe pulses. A short-lived region of photoinduced bleaching was observed in the differential transmission spectra at wavelengths shorter than the pump wavelength. The excitation of coherent phonon states with a spectrum corresponding to nanocrystalline silicon with an admixture of a disordered phase was observed. The relaxation of electronic excitation was found to slow down in the spectral region where the amplitude of excited coherent vibrations was maximal.

PACS numbers: 78.66.Ob; 63.20.-e

Porous silicon (PS) has been attracting considerable attention because of the photoluminescence (PL) and electroluminescence properties recently discovered for this material in the visible spectral region [1]. However, up to now, there has been much debate over the nature and mechanism of PS luminescence. The radiative hole–electron recombination from the size-quantization levels in silicon nanocrystals [1], the radiative recombination involving surface states [2], and the radiative transitions in silicon oxide [3] or amorphous silicon, which can be present in PS films [4], have been suggested as an explanation.

An analysis of the experimental data on the photoluminescence properties and their association with the PS structure has shown [4] that the vast majority of these data can be satisfactorily explained by introducing the size-quantization levels. However, such an interpretation raises debates, primarily because of the following two facts: first, there is a large scatter in the results obtained by different researchers, so that they can only be qualitatively compared with each other; second, the size-quantization levels in porous silicon have not yet been identified with certainty. The first item is due to a multiparameter dependence of the PS properties on the preparation, keeping, and investigation conditions, while the second item is due to a large dispersion of nanocrystal sizes in PS.

Due to the complexity of interpreting the photoluminescence properties of PS, its structural, optical, and nonlinear optical properties, as well as the mechanisms of electrochemical etching have been much investigated. Measurements of the linear and nonlinear optical properties and, in particular, the nonlinear time-resolved transmission and reflectance spectra can complement the PL data. However, the use of a size-quantization model alone for the explanation of some of the experimental facts obtained in the nonlinear optical investigations of PS, as in the PL experiments [5], also encounters certain difficulties. Among these are the presence of several fast (picosecond and subpicosecond) and slow (nanosecond and microsecond) components in the nonlinear transmission spectra and the radical difference in the character of the spectra obtained using different pump techniques [6, 7]. This suggests that the photoinduced processes in PS likely have a rather complicated nature and depend essentially on the excitation conditions. On the whole, the investigations into the nonlinear optical and relaxational properties are as yet inadequate to give a complete picture of photoinduced processes occurring both in PS and in other silicon-based nanostructures.

The time-resolved pump–probe technique has become a powerful tool in studying the nature of excited states, their structure, and relaxation dynamics [6–10]. The use of the pump–probe technique with supercontinuum probing and femtosecond time resolution can provide additional possibilities [8–10]. With an exciting pulse duration shorter than half the period of phonon vibrations, one can observe the effects associated, e.g., with the excitation of coherent and squeezed phonon states [11] and trace their spectral and temporal dynamics, thereby substantially facilitating the interpretation of the excitation relaxation mechanisms in PS.

This work reports the results of studying the dynamics of photoinduced PS spectra recorded by the pump–supercontinuum probe technique [8–10] with a high

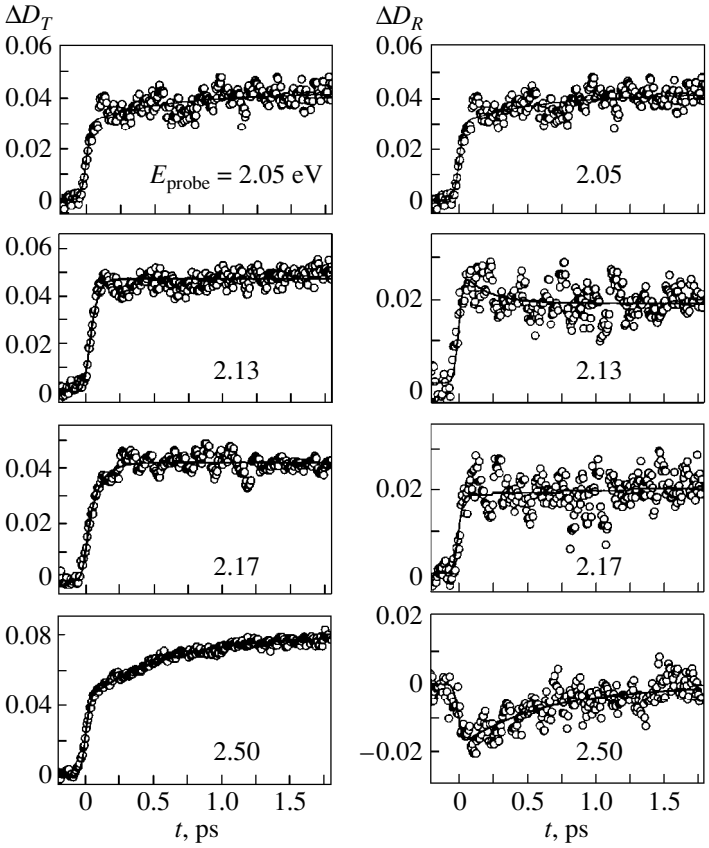

Fig. 1. Differential optical density ΔD_T (left) and ΔD_R (right) as functions of the time delay between the pump ($\hbar\omega_{pump}$ = 2.34 eV) and probe ($\hbar\omega_{probe}$ = 2.05, 2.13, 2.15, and 2.5 eV) pulses at room temperature. Circles are for the experimental data, and solid lines correspond to the biexponential fitting.

time resolution. The excitation of coherent phonon states was observed in porous silicon. The spectrum of the coherent phonon states corresponds to nanocrystalline silicon with an admixture of a disordered phase. The relaxation of electronic excitation was found to slow down in the spectral regions where the amplitude of coherent vibrations was maximal. The differential transmission spectra of the femtosecond-excited porous silicon films showed the presence of a short-lived photoinduced bleaching region in their short-wavelength part relative to the pump wavelength.

The PS samples were prepared by anodizing KES 0.01 (111) crystal silicon substrate commercially fabricated for the microelectronics industry. An HF(49%) : ethanol (1 : 1) electrolyte was used. The anodization was run for 20 min in a two-compartment fluoroplastic electrochemical cell in the dark at a current density of 40 mA/cm^2, with a step increase to 100 mA/cm^2 at the stage of film separation from the substrate. The separated film was washed with ethanol, dried in a flow of dry air, and fixed at a diaphragm. Measurements were made after aging the films under ambient conditions for 7–8 months to stabilize their properties.

The samples were excited by optical femtosecond ($\tau \approx 50$ fs) pump pulses with photon energy of $\hbar\omega_{pump}$ = 2.34 eV and repetition rate of 2 Hz. The pump energy was varied within 0.4– 2.0 μJ. The pump-beam spot was 150 μm in diameter. The probing was accomplished using a supercontinuum (1.6–3.2 eV) femtosecond pulse formed upon the passage of a portion of the laser pulse through a fused quartz plate. The resulting spectrum was recorded in the wavelength range 380–780 nm ($\hbar\omega_{probe}$ = 1.6–3.2 eV) on a polychromator with a photodiode array containing 512 elements and providing a resolution of 1.5 nm. The duration at the half-height of a pump–probe cross-correlation function was equal to $\tau_{cc} \approx 70$ fs for all probe wavelengths. The probe-beam spot was 100 μm in diameter. According to our estimates, the absolute error of recording ΔD_T and ΔD_R did not exceed 0.003. All measurements were carried out at room temperature. The steady-state absorption spectrum was monitored [10] to make sure that no irreversible changes happened to the samples during the experiments. The time evolution of the photoinduced response was studied by varying the delay time between the pump and probe pulses up to 2.5 ps with a step of 7 fs. The resulting signal was averaged over

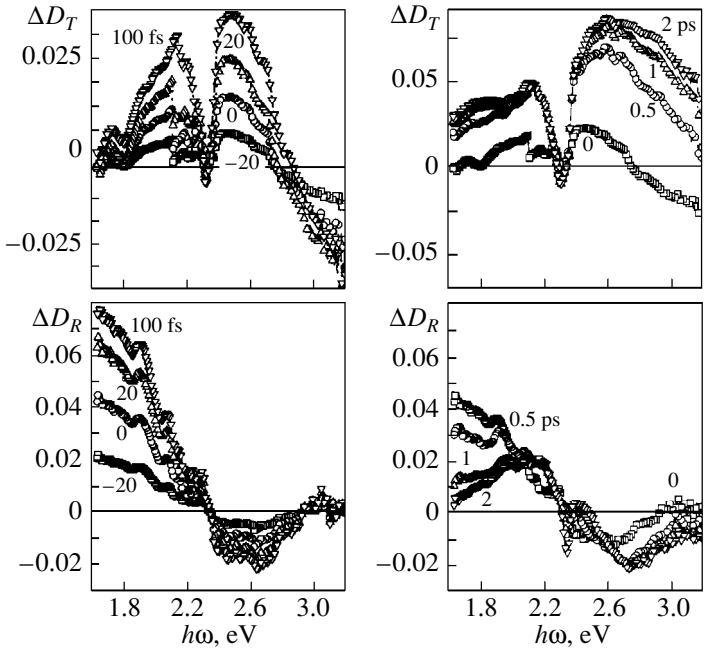

Fig. 2. Differential transmittance ΔD_T and reflectance ΔD_R spectra of the PS film for different delay times.

eight measurements. The necessary time corrections were applied to the spectra. According to our estimates, the correction accuracy was 10 fs. A detailed description of the experimental setup and the methods of processing experimental results can be found in [8–10].

Specifically, the differential transmission optical density $\Delta D_T = \log(T^*/T_0)$ and reflectance $\Delta D_R = \log(R^*/R_0)$ spectra were experimentally measured for a PS film (T^* and R^* are the excited-state transmittance and reflectance, respectively, and T_0 and R_0 are the same for the ground state). To simplify the analysis, the experimental information on $\Delta D_T(\omega, t)$ and $\Delta D_R(\omega, t)$ is represented in the form of time (Fig. 1) and energy (Fig. 2) dependences at a fixed value of the other of these parameters. To apply time corrections to the differential spectra (ΔD_T and ΔD_R) and determine relaxation rates, the experimental signal $\Delta D_{\exp}(\omega, t)$ was fitted to a biexponential response function, in which the fast relaxation processes were characterized by the $\gamma_1(\omega)$ rate and the slower processes, by the $\gamma_2(\omega)$ rate [10].

Let us consider the results obtained. Figure 1 shows the differential optical density ΔD_T (left) and ΔD_R (right) as functions of the time delay between the pump ($\hbar\omega_{\text{pump}} = 2.34$ eV) and probe ($\hbar\omega_{\text{probe}} = 2.05$, 2.13, 2.15, and 2.5 eV) pulses. The circles correspond to the experimental data, and the solid lines are for fitting these data to a biexponential function [10]. The differential optical-density ΔD_T (upper panels) and reflectance ΔD_R (lower panels) spectra are displayed in Fig. 2 for different pump–probe time delays. A dip at 2.34 eV corresponds to the energy of pump photons. To obtain numerical values for the relaxation rates, each of the 512 kinetics was fitted to a biexponential function convoluted with the pump–probe cross-correlation function [10]. The spectrum $\gamma_1(\omega)$ of the relaxation rates is shown in Fig. 3.

The differential transmission spectra $\Delta D_T(\omega, t)$ were found to exhibit nonmonotonic spectral behavior (Fig. 2, upper part). One can recognize a low-frequency induced-absorption region [$\Delta D_T(\omega, t) > 0$] with a maximum at $\hbar\omega \sim 2.5$ eV and a high-frequency induced-transmission region [$\Delta D_T(\omega, t) < 0$] with a maximum near $\hbar\omega \sim 3.1$ eV. It is seen that the induced transmission rapidly relaxes and disappears 500 fs after the excitation. From this time on, only the induced absorption ($\Delta D_T(\omega, t) > 0$) with a maximum near $\hbar\omega \sim 2.5$ eV is observed over the entire spectrum.

It is also seen that the reflectance spectra $\Delta D_R(\omega, t)$ (Fig. 2, bottom part) exhibit nonmonotonic behavior, with $\Delta D_R(\omega, t) > 0$ at photon energies lower than $\hbar\omega_{\text{pump}}$ and $\Delta D_R(\omega, t) < 0$ above $\hbar\omega_{\text{pump}}$. In the range 3.0–3.1 eV, the sign of the differential reflectance changes again and $\Delta D_R(\omega, t)$ slightly exceeds zero. One can also see that the low-frequency band contains a fast component at frequencies $\hbar\omega < 1.9$ eV, which disappears within 500 fs to give way to a long-lived $\Delta D_R(\omega, t) > 0$ band with a maximum at 2.1 eV. In the first 100 fs, the high-frequency $\Delta D_R(\omega, t) < 0$ band only changes its amplitude (maximum at 2.5 eV), whereupon it shifts to higher energies (maximum at 2.8 eV) within 500 fs. This is accompanied by an increase in the $\Delta D_R(\omega, t)$

amplitude. As a result, a narrow region with $\Delta D_R(\omega, t) > 0$ in the short-wavelength part of the spectrum disappears within 500 fs after excitation (or shifts to the shorter wavelengths beyond the observation region). It is worth noting that the induced transmittance [$\Delta D_R(\omega, t) < 0$] observed in the differential optical-density spectrum occurs precisely in the same spectral region and disappears in the same time period. In this work, only the most prominent features of the phenomenon will be considered.

One can also see in Fig. 2 that the relaxation of induced absorbance slows down near $\hbar\omega_{probe} = 1.95$ and 2.5 eV, as is also evident from the time-dependent curves in Fig. 1 and frequency-dependent fast component $\gamma_1(\omega)$ in Fig. 3 (where the pump region near 2.34 eV is cut off). The relaxation rate $\gamma_1(\omega)$ is virtually constant throughout the whole frequency range (2 ps^{-1}), except for the regions near 1.95 and 2.5 eV. A plausible explanation for such behavior is that the induced absorption, on the whole, proceeds from excited carriers exhibiting a quasicontinuum energy spectrum, because such a complicated system as porous silicon possesses a wide variety of allowed energy transitions, e.g., in silicon nanocrystals, in residual products of electrochemical reaction, in adsorbate, and surface localized states. It should also be remembered that these systems can interact with each other. As to the $\hbar\omega_{probe}$ regions near 1.95 and 2.5 eV where the relaxation slows down, one can assume that they are associated with the energetically isolated longer lived levels; e.g., they are due to the contribution of the size-quantization levels of the selectively excited silicon nanocrystals. It should be noted that the positions of the slow-relaxation bands coincide with the positions of the orange–red (1.95 eV) and green–blue (2.5 eV) bands in the known photoluminescence spectra of PS [5].

On the whole, the time dynamics can be characterized by two relaxation times: short time (1 ps in the range of 1.95 eV and 600 fs in the range of 2.5 eV) and longer times on the order of tens of picoseconds. The rate of the longer component was approximately constant and equal to 0.06 ps^{-1}; i.e., the relaxation time was 16 ps, in accordance with the data reported for porous silicon earlier in [6, 7].

Another important feature is seen in Fig. 1, where the time dependences are shown for $\Delta D_T(\omega, t)$ and $\Delta D_R(\omega, t)$ at fixed $\hbar\omega_{probe}$ values. In these curves, one can recognize an additional high-frequency modulation against the background of the exponential relaxation. Such a modulation is known to occur upon the excitation of coherent phonon states by femtosecond pulses [8, 10, 11]. The vibrational spectrum in the entire probe region was obtained by Fourier analysis of the differential photoinduced response $\Delta D_{exp}(\omega, t) - \Delta D_{fit}(\omega, t)$. The spectra were corrected with allowance made for the convolution of the observed response and the pump pulse shape [9, 10]. Figure 4 shows the resulting spectrum averaged over the probe range of 1.75–2.15 eV, where these oscillations are most pronounced. Two peaks are prominent, of which the major maximum occurs at a frequency of 518 cm^{-1}, while the minor one occurs at 480 cm^{-1}. The first peak is shifted to lower frequencies from the position of the Raman line in crystalline silicon (521 cm^{-1}); and, hence, it is indicative of the presence of silicon nanocrystallites [12], while the second peak is evidence for the presence of a disordered silicon phase [13]. These oscillations agree well with the data obtained earlier in [14, 15]. It should be noted that the excitation of coherent vibrations is $\hbar\omega$-selective; namely, they are most intense at frequencies cor-

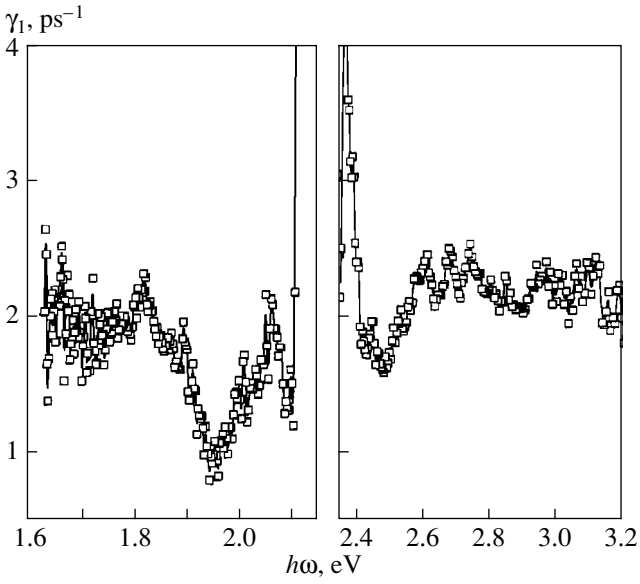

Fig. 3. Frequency-dependent relaxation rate $\gamma_1(\hbar\omega_{probe})$. Pump power $I_{pump} = 10^{11}$ W/cm^2 and $\hbar\omega_{pump} = 2.34$ eV.

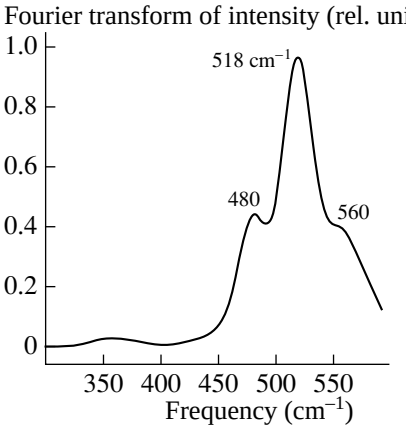

Fig. 4. Amplitude of coherent oscillations in the frequency–photon energy plane. Pump power $I_{pump} = 10^{11}$ W/cm^2 and $\hbar\omega_{pump} = 2.34$ eV.

responding to the positions of slow-relaxation bands. This can be regarded as an additional argument in favor of the assumption that the relaxation slowdown is associated with the electronic excitations both in the silicon nanocrystals (518 cm^{-1}) and in a disordered phase (480 cm^{-1}).

Thus, the excitation of coherent phonon states was observed in porous silicon for the first time. The spectrum of coherent phonon states corresponds to nanocrystalline silicon with an admixture of a disordered phase. The relaxation of electronic excitation is found to slow down at spectral regions where the amplitude of excited coherent vibrations is maximal, allowing them to be assigned to the localized levels in silicon nanocrystals present in PS. In the case of femtosecond excitation, the differential transmission spectra of the porous silicon films show the presence of a short-lived photoinduced bleaching region at wavelengths shorter than the pump wavelength. This property is of importance for optoelectronics, where this material can be used in ultrafast optical switches. These effects are also of considerable interest because of their possible use for optical confinement (slow 15- to 20-ps component).

This work was supported in part by the Russian Foundation for Basic Research the Program "Physics of Solid-State Nanostructures."

REFERENCES

1. A. G. Cullis, L. T. Canham, and P. D. J. Calcott, J. Appl. Phys. **82**, 909 (1997); L. T. Canham, Appl. Phys. Lett. **57**, 1046 (1990).
2. F. Koch, Mater. Res. Soc. Symp. Proc., No. 298, 319 (1993).
3. A. Roy, A. Chainani, D. D. Sarma, and A. K. Sood, Appl. Phys. Lett. **61**, 1655 (1992).
4. S. M. Prokes, J. Appl. Phys. **73**, 407 (1993).
5. H. Koyama and N. Koshida, Solid State Commun. **91**, 239 (1994).
6. V. Klimov, D. McBranch, and V. Karavanskiĭ, Phys. Rev. B **52**, R16989 (1995).
7. P. Maly, F. Trojanek, A. Hospodkova, *et al.*, Solid State Commun. **89**, 709 (1994).
8. V. M. Farztdinov, Yu. E. Lozovik, Yu. A. Matveets, *et al.*, Phys. Rev. Lett. **67**, 3860 (1991); V. M. Farztdinov, A. L. Dobryakov, S. A. Kovalenko, *et al.*, Phys. Rev. B **56**, 4176 (1997); Yu. E. Lozovik, A. L. Dobryakov, S. A. Kovalenko, and N. P. Ernsting, Phys. Lett. A **223**, 303 (1996).
9. S. A. Kovalenko, A. L. Dobryakov, J. Ruthmann, and N. P. Ernsting, Phys. Rev. A **59**, 2369 (1999).
10. A. L. Dobryakov, S. A. Kovalenko, V. Karavanskiĭ, *et al.*, Phys. Scr. **60** (1999); A. L. Dobryakov, S. A. Kovalenko, D. V. Lisin, *et al.*, Izv. Ross. Akad. Nauk, Ser. Fiz. (in press).
11. R. Merlin, Solid State Commun. **102**, 207 (1997).
12. *Phonons in Semiconductor Nanostructures*, Ed. by J.-P. Leburton, J. Pascual, and C. S. Torres (Kluwer, Dordrecht, 1993); *Light Scattering in Semiconductor Structures and Superlattices*, Ed. by D. J. Lockwood and J. F. Young (Plenum, New York, 1991).
13. A. Roy, K. Jayaram, and A. K. Sood, Solid State Commun. **89**, 229 (1994).
14. D. J. Lockwood, A. Wang, and B. Bryskiewicz, Solid State Commun. **89**, 587 (1994).
15. Md. N. Islam, P. S. Dobal, H. D. Bist, and S. Kumar, Solid State Commun. **107**, 43 (1998).

Translated by V. Sakun

JETP Letters, Vol. 71, No. 7, 2000, pp. 303–306. From Pis'ma v Zhurnal Éksperimental'noĭ i Teoreticheskoĭ Fiziki, Vol. 71, No. 7, 2000, pp. 437–442.

CONDENSED MATTER

Magnetic Field–Temperature Phase Diagram of the Organic Conductor α-(BEDT-TTF)$_2$KHg(SCN)$_4$[1]

P. Christ*, W. Biberacher*, M. V. Kartsovnik*, **, E. Steep*, E. Balthes***, H. Weiss***, and H. Müller******

** Walther-Meissner-Institut, D-85748 Garching, Germany*

*** Institute of Solid State Physics, Russian Academy of Sciences, Chernogolovka, Moscow region, 142432 Russia*

**** High Magnetic Field Laboratory, MPI-FKF and CNRS, F-38042 Grenoble, France*

***** European Synchrotron Radiation Facility, F-38043 Grenoble, France*

Received March 1, 2000

We present systematic magnetic torque studies of the "magnetic field–temperature" phase diagram of the layered organic conductor α-(BEDT-TTF)$_2$KHg(SCN)$_4$ at fields nearly perpendicular and nearly parallel to the highly conducting plane. The shape of the phase diagram is compared to that predicted for a charge-density-wave system in a broad field range. © *2000 MAIK "Nauka/Interperiodica".*

PACS numbers: 75.30.Kz; 71.30.+h; 71.45.Lr; 73.61.Tm

Organic metals α-(BEDT-TTF)$_2$MHg(SCN)$_4$, where M = K, Tl, or Rb [1], have attracted much attention in the last decade due to their exotic low-temperature electronic state. They are characterized by a layered crystal structure and a unique coexistence of quasi-one-dimensional (Q1D) and quasi-two-dimensional (Q2D) conducting bands [1]. The transition into the low-temperature state is associated with a $2k_F$ nesting instability of the Q1D part of the Fermi surface. Indeed, experiments on the angle-dependent magnetoresistance oscillations [2–5] have revealed a significant change in the electronic system due to a periodic potential with the wave vector close to the doubled Fermi wave vector of the Q1D band. On the other hand, studies of the magnetization anisotropy [6, 7] and μSR [8] give evidence for a low amplitude modulation of the magnetic moment, suggestive of a spin-density wave (SDW). Many of the striking anomalies displayed by these compounds in a magnetic field can be fairly well explained by the density-wave instability, taking into account the coexistence of the Q1D and Q2D Fermi surfaces (see, e.g., [3–5, 9, 10]). However, there remain several questions which can hardly be understood within the SDW model. One of the important questions concerns the effect of a magnetic field on the low-temperature state.

It is known that a magnetic field applied perpendicular to the direction of the spin polarization may stimulate SDW formation in systems with imperfectly nested Fermi surfaces due to effective reduction of the electron motion to one dimension [11, 12]. This orbital effect leads to a slight increase in the SDW transition temperature, as was shown for a Q1D conductor (TMTSF)$_2$PF$_6$ [13]. The situation with the α-(BEDT-TTF)$_2$MHg(SCN)$_4$ salts is rather controversial in this respect. In agreement with the SDW model, Sasaki *et al.* [14] reported that the transition temperature T_p in α-(BEDT-TTF)$_2$KHg(SCN)$_4$ increased in a magnetic field perpendicular to the spin polarization plane (which is the highly conducting *ac*-plane in this compound [15]). On the contrary, other numerous experiments suggest a reduction of T_p in a magnetic field. Some authors [16, 17] claim that the low-temperature state is completely suppressed in this salt and the normal metallic state is restored above the so-called *kink* transition at $B_{\mathrm{kink}} \simeq 24$ T. On the other hand, several works suggest that a new phase, different from the normal one, emerges above B_{kink} [18, 19]. Based on the shape of the "magnetic field–temperature" (*B*–*T*) phase diagrams [18, 19], Biskup *et al.* [19] proposed a phase transition driven by a charge-density wave (CDW) rather than SDW instability.

It should be noted, that the studies of the high-field region of the *B*–*T* diagram of the α-(BEDT-TTF)$_2$MHg(SCN)$_4$ compounds have been mostly done by use of magnetoresistance technique. Obviously, such experiments are difficult to interpret unambiguously in terms of phase transitions. Therefore, a detailed investigation of thermodynamic properties is necessary in order to establish the phase boundaries. So far only few magnetization data at fields above 15 T have been presented in two works [14, 18]. However, the conclusions made in these works concerning the field effect on the transition temperature contradict each other. To elucidate the problem, we have carried out a systematic study of the *B*–*T* phase diagram of

[1] This article was submitted by the authors in English.

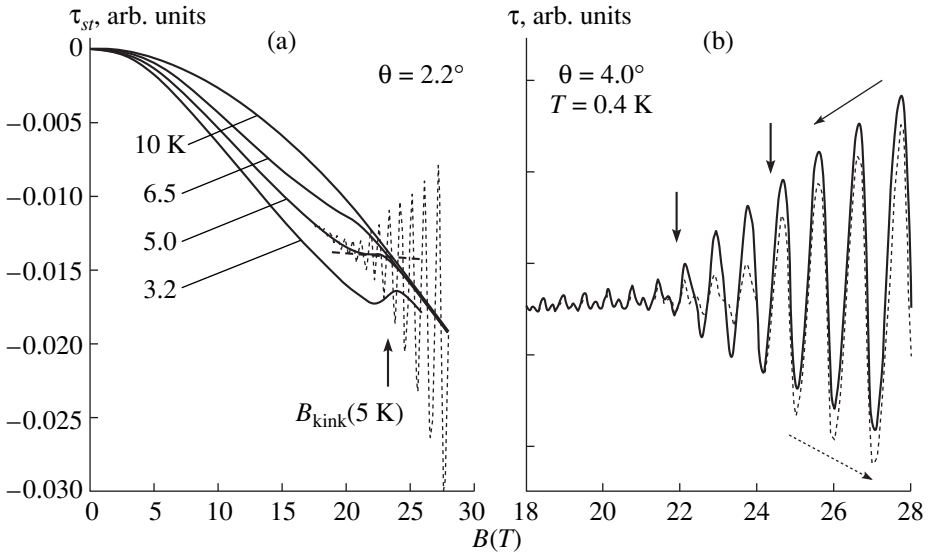

Fig. 1. Torque as a function of a magnetic field applied nearly perpendicular to the *ac*-plane: (a) steady part of the torque at different temperatures; the dotted curve represents the total signal from the sample, with the dHvA oscillations at $T = 5.0$ K; (b) up (dotted line) and down (solid line) field sweeps of the torque at low temperature.

α-(BEDT-TTF)$_2$KHg(SCN)$_4$ by means of magnetic torque experiments.

Several high-quality samples chosen for the experiment were grown by the standard electrochemical method [20] and had a typical mass of 100 to 350 μg. A cantilever beam magnetometer [7] was used to measure the torque in fields nearly perpendicular and nearly parallel to the highly conducting *ac*-plane. The measurements were performed at temperatures between 0.4 and 18 K in magnetic fields up to 28 T produced at the High Magnetic Field Laboratory in Grenoble, France.

We first focus on field directions almost perpendicular to the layers. Typical field dependences of the steady part of the torque $\tau_{st}(B)$ are shown in Fig. 1a for the angle θ between the magnetic field and the normal to the *ac*-plane equal to 2.2°. At high temperatures ($T \geq 8$ K), we find an almost temperature-insensitive quadratic dependence of the torque on magnetic field. On lowering the temperature below 8 K, the quadratic term increases at small fields, but above 4 T the dependence becomes weaker than quadratic, and at high fields the curves bend to merge with the high-temperature curve. The field at which the torque returns to its normal behavior coincides with the kink field B_{kink} as determined in other experiments [14, 16–19]. In addition to the steady part of the torque, de Haas-van Alphen (dHvA) oscillations were observed. At 10 K these oscillations were resolved only at the highest fields; but at 5.0 K their amplitude was already comparable to $\tau_{st}(B)$, as shown by a dashed line in Fig. 1a. To extract $\tau_{st}(B)$, we used a Fourier filter. In contrast to the measurements at higher temperatures, the curve at 3.2 K does not return to the high-temperature part at B_{kink} but stays below. For temperatures below 3 K, the dHvA amplitude becomes so strong that the steady torque cannot be extracted reliably any more. In Fig. 1b we show a trace of a field sweep from 18 T to 28 T and back made at 0.4 K. There is a clear transition from a low-field state (characterized by a splitting of the oscillation amplitude) to a high-field state (characterized by a higher oscillation amplitude and the absence of splitting). This transition shows a strong hysteresis of the dHvA amplitude in the field interval marked by fat arrows in Fig. 1b. Furthermore, there is a significant shift between up and down sweep curves in the high-field part, indicating a complex magnetic state.

To clarify the latter point, we performed temperature sweeps at constant fields. For these experiments it is of crucial importance to suppress the influence of the oscillatory part [18]. We therefore performed these sweeps at field values at which the dHvA contribution to the temperature dependence is nearly zero. The results are shown in Fig. 2a. Despite a small remanent dHvA contribution, there is still a clear transition into a new state even at the highest field.

In order to determine anisotropy effects in the phase diagram, we performed torque experiments at fields almost parallel to the layer plane. The phase transition is clearly seen in temperature sweeps. Typical examples taken at different fields at $\theta = 87.5°$ are given in Fig. 2b. The field dependence of the torque below 4 K shows a complex behavior with a strong hysteresis between up and down field sweeps [21]. This behavior is drastically different from the feature observed at the kink transition at low angles. An example of a field sweep at 1.3 K is shown in the inset in Fig. 2b.

The results of our studies can be summarized by plotting a *B*–*T* phase diagram, as shown in Fig. 3. Here

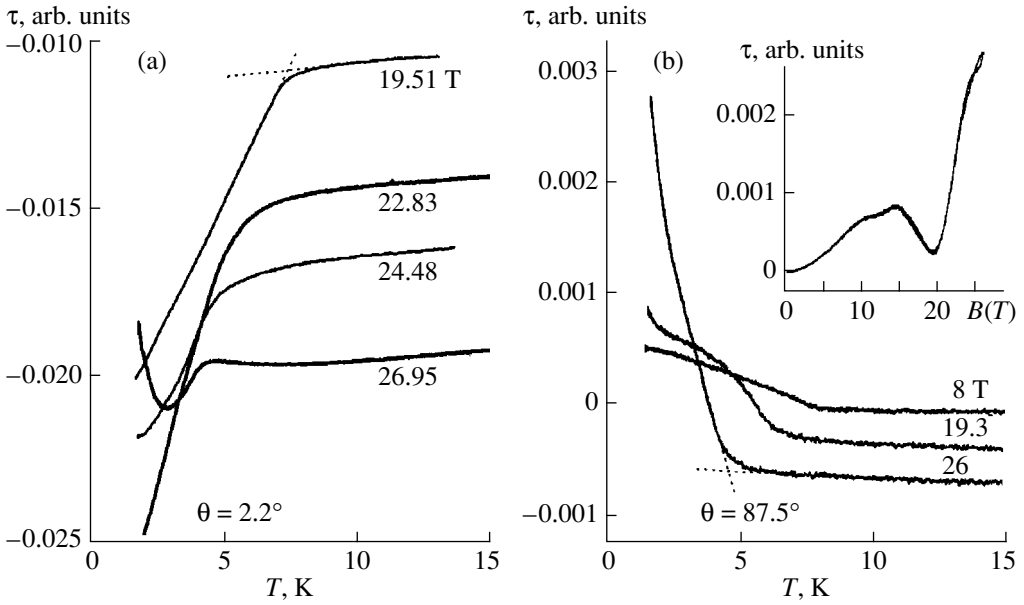

Fig. 2. Temperature sweeps of the torque at θ = (a) 2.2° and (b) 87.5° at different fields. The inset shows the field dependence of the torque at θ = 87.5°, T = 1.3 K.

the data obtained on four samples having slightly different T_p (ranging from 8.0 to 8.4 K) are presented. That is why the temperature and field are given in reduced units $T/T_p(0)$ and $\mu_B B/k_B T_p(0)$, respectively [here, $T_p(0)$ is the extrapolated critical temperature at zero field]. The definition of the transition points is illustrated in Figs. 1 and 2.

The low-angle data in Fig. 3 are qualitatively consistent with the B–T diagrams obtained from earlier magnetoresistance [18, 19] and torque [18] measurements in tilted fields. Firstly, the transition temperature continuously decreases with increasing field; secondly, the low-temperature state is different from the normal nonmagnetic state even above the kink transition. Quantitatively, our data are in perfect agreement with those obtained from specific heat measurements at $B \le 14$ T [22]. These results are obviously in conflict with the SDW model. On the other hand, they can be compared to what is expected for a CDW [23]. At low field, the CDW_0 phase with an optimal zero-field wave vector is stable below T_p. As the field increases, the Zeeman splitting of the subbands with antiparallel spins leads to the deterioration of the nesting conditions and, consequently, suppression of T_p [21]. However, when the Zeeman splitting energy reaches the value of the zero-temperature energy gap, the formation of a spatially modulated CDW_x state with a longitudinally shifted wave vector is expected. This state is analogous to the Fulde–Ferrel–Larkin–Ovchinnikov state predicted for superconductors [25] and persists to considerably higher fields than the conventional CDW_0. The phase diagram proposed by Zanchi *et al.* [23] for a CDW system with perfect nesting is shown by dashed lines in Fig. 3. Apart from different field scales, the phase diagrams are remarkably similar to each other.

Assuming the CDW model, the deviation of the actual phase boundary for fields nearly perpendicular to the plane to higher temperatures at $T_p/T_p(0) > 0.6$ can be ascribed to a significant orbital effect of the magnetic field. This effect is important for an imperfectly nested

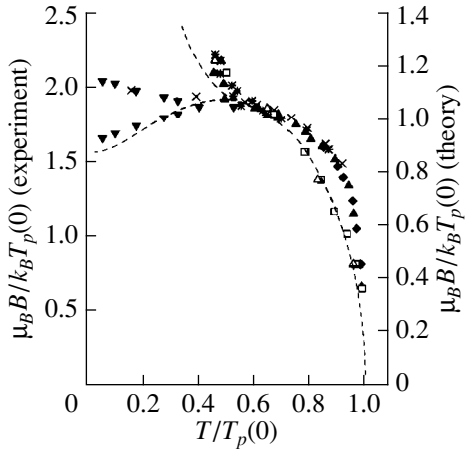

Fig. 3. Phase diagram of α-$(BEDT\text{-}TTF)_2KHg(SCN)_4$. Different symbols correspond to the transition points obtained from the $\tau_{st}(T)$ sweeps at θ = 2.2° (stars, sample no. 1), 6.5° (solid diamonds, sample no. 2), 11.8° (solid up-triangles, sample no. 3), 87.5° (open squares, sample no. 1), and 89.5° (open up-triangles, sample no. 1); $\tau_{st}(B)$ sweeps at θ = 2.2° (crosses, sample no. 1); and characteristic changes in the dHvA signal at θ = 4.0° (solid down-triangles, sample no. 4). The dashed lines represent the phase diagram predicted for a CDW system with a perfectly nested Fermi surface [23].

Fermi surface and leads to a relative increase in T_p [12, 23]. In our case, when the warping of the open Fermi surface sheets is much stronger within the *ac*-plane than in the interlayer direction, the orbital effect should be anisotropic: its contribution decreases as the angle θ approaches 90°. Indeed, the critical temperature of the transition into the low-temperature low-field state is found to be systematically lower at $\theta \simeq 90°$, lying perfectly on the theoretical line (Fig. 3). This implies that the orbital effect is absent for the in-plane field direction.

In the high-field region, the phase lines determined at different field orientations seem to converge, suggesting an isotropic effect of the magnetic field on the transition temperature into the low-temperature high-field state. For a definite conclusion, more detailed studies at different angles are needed.

The considerable difference between the field scale in the phase diagram obtained from the experiment and that predicted by the CDW model is not very surprising. Indeed, the model calculations [23] are made within a mean-field approximation neglecting fluctuation effects. The latter may significantly lower $T_p(0)$ with respect to the mean-field value. Furthermore, the imperfect nesting which likely occurs in the present system has a stronger suppressing effect on $T_p(0)$ than on the critical field [23]. Both these factors lead to an underestimation of the actual critical fields.

Finally, we note that the field dependence of the torque at high angles has no simple explanation within the proposed model. The nonmonotonic torque with a hysteresis between up and down field sweeps observed at $\theta \gtrsim 60°$ [21] is reminiscent of multiple phase transitions. As the angle approaches 90°, the features become less pronounced, although they still persist to angles as high as 88°–89° (see inset in Fig. 2b). In principle, an additional phase transition into a CDW_y state with a transversally shifted wave vector may be expected at high angles at which the orbital effect is sufficiently suppressed [23]. Still, it cannot account for the whole structure of the torque at high angles and its complicated angular dependence. Obviously, the applied model [23] is too oversimplified to explain all the field effects. For a more adequate description, it seems very important to include the Q2D band into consideration. In particular, it was recently shown that oscillations of the chemical potential due to the quantization of the 2D orbits have a significant impact on the CDW gap [26]. On the other hand, the magnetization anisotropy itself, revealing an "easy-plane" spin polarization at low temperatures [15], indicates a nontrivial magnetic structure linked to the probable CDW.

In conclusion, we have presented a *B*–*T* phase diagram of α-(BEDT-TTF)$_2$KHg(SCN)$_4$ built on the basis of magnetization measurements. The shape of the diagram and the effect of the field orientation are suggestive of a CDW formation accompanied by imperfect nesting of the Q1D part of the Fermi surface. If this is true, the high-field phase would represent the first example of a CDW with a spatially modulated wave vector.

We thank A. Bjelis for very useful discussions. The work was supported in part by the TMR Program of the European Community (contract no. ERBFMGECT950077).

REFERENCES

1. H. Mori, S. Tanaka, M. Oshima, *et al.*, Bull. Chem. Soc. Jpn. **63**, 2183 (1990).
2. M. V. Kartsovnik, A. E. Kovalev, and N. D. Kushch, J. Phys. I **3**, 1187 (1993).
3. A. E. Kovalev, M. V. Kartsovnik, R. P. Shibaeva, *et al.*, Solid State Commun. **89**, 575 (1994).
4. T. Sasaki and N. Toyota, Phys. Rev. B **49**, 10120 (1994).
5. J. Caulfield, S. J. Blundell, M. S. L. du Croo de Jongh, *et al.*, Phys. Rev. B **51**, 8325 (1995).
6. T. Sasaki, H. Sato, and N. Toyota, Synth. Met. **41–43**, 2211 (1991).
7. P. Christ, W. Biberacher, H. Müller, and K. Andres, Solid State Commun. **91**, 451 (1994).
8. F. L. Pratt, T. Sasaki, N. Toyota, and K. Nagamine, Phys. Rev. Lett. **74**, 3892 (1995).
9. M. V. Kartsovnik, D. V. Mashovets, D. V. Smirnov, *et al.*, J. Phys. I **4**, 159 (1994).
10. R. H. McKenzie, G. J. Athas, J. S. Brooks, *et al.*, Phys. Rev. B **54**, R8289 (1996).
11. L. P. Gor'kov and A. G. Lebed, J. Phys. Lett. **45**, L433 (1984).
12. G. Montambaux, Phys. Rev. B **38**, 4788 (1988).
13. G. M. Danner, P. M. Chaikin, and S. T. Hannahs, Phys. Rev. B **53**, 2727 (1996).
14. T. Sasaki, A. G. Lebed, T. Fukase, and N. Toyota, Phys. Rev. B **54**, 12969 (1996).
15. P. Christ, W. Biberacher, W. Bensch, *et al.*, Synth. Met. **86**, 2057 (1997).
16. A. A. House, S. J. Blundell, M. M. Honold, *et al.*, J. Phys.: Condens. Matter **8**, 8829 (1996).
17. J. S. Brooks, X. Chen, S. J. Klepper, *et al.*, Phys. Rev. B **52**, 14457 (1995).
18. M. V. Kartsovnik, W. Biberacher, E. Steep, *et al.*, Synth. Met. **86**, 1933 (1997).
19. N. Biskup, J.A.A.J. Perenboom, J. S. Brooks, and J. S. Qualls, Solid State Commun. **107**, 503 (1998).
20. H. Müller and Y. Ueba, Synthesis **9**, 853 (1993).
21. P. Christ, W. Biberacher, A. G. M. Jansen, *et al.*, Synth. Met. **70**, 823 (1995).
22. A. E. Kovalev, H. Müller, and M. V. Kartsovnik, Zh. Éksp. Teor. Fiz. **113**, 1058 (1998) [JETP **86**, 578 (1998)].
23. D. Zanchi, A. Bjelis and G. Montambaux, Phys. Rev. B **53**, 1240 (1996).
24. W. Dietrich and P. Fulde, Z. Phys. **265**, 239 (1973).
25. P. Fulde and R. A. Ferrel, Phys. Rev. A **135**, 550 (1964); A. I. Larkin and Yu. N. Ovchinnikov, Zh. Éksp. Teor. Fiz. **47**, 1136 (1964) [Sov. Phys. JETP **20**, 762 (1964)].
26. N. Harrison, Phys. Rev. Lett. **83**, 1395 (1999).

JETP Letters, Vol. 71, No. 7, 2000, pp. 307–309. Translated from Pis'ma v Zhurnal Éksperimental'noĭ i Teoreticheskoĭ Fiziki, Vol. 71, No. 7, 2000, pp. 443–447.

CONDENSED MATTER

Physical Implementation of Three-Qubit Gates on a Separate Quantum Particle

A. R. Kessel' and V. L. Ermakov

Zavoĭskiĭ Physicotechnical Institute, Kazan Scientific Center, Russian Academy of Sciences, Sibirskiĭ trakt 10/7, Kazan 29, 420029 Tatarstan, Russia

e-mail: wrmakov@sci.kcn.ru

Received February 15, 2000

A virtual spin formalism is suggested to demonstrate that a single quantum particle possessing eight suitable discrete energy levels can be used for storing three information qubits and organizing on them a universal set of logical operations that are necessary for constructing an arbitrary quantum algorithm. The formalism can be practically implemented on a nuclear spin 7/2 subjected to resonance rf pulses. A single-pulse realization is found for all quantum gates of a universal set, including a three-qubit gate. *© 2000 MAIK "Nauka/Interperiodica".*

PACS numbers: 03.67.Lx; 03.67.Hk; 76.60.-k

It was shown in the theory of computation that a classical reversible computer can be constructed on a basis of a universal three-qubit controlled-controlled-NOT (CCNOT) gate [1]. In quantum informatics, the CCNOT gate is generalized as a controlled-controlled unitary transformation (CCUT) gate [2]. The CCUT is a three-qubit gate, in which the controlled qubit is subjected to an arbitrary unitary rotation if and only if two controlling qubits are in the $|1\rangle$ state. The CCUT gate transforms into the CCNOT gate upon rotations through a certain angle [$\varphi_{mn} = \pi$, see below (4)]. However, it was found that the CCUT operation is hard to realize, because three-body interactions do not exist in nature. An indirect method was found in [3]: it turned out that the CCUT can be assembled from five two-qubit gates. This way was realized by a sequence of several NMR pulses in a system of three spins of 1/2 {equations (38) and (39) in [4]}.

In this work, a virtual spin formalism suggested in [5] is used to practically implement the CCUT gate in the simplest way, viz., by means of a single pulse on a single quantum particle. The advantages of practical use of such a device are beyond question.

Gate representation by three spins of 1/2 in quantum informatics. To construct three-qubit gates, quantum informatics exploits Hilbert space Γ that is organized as a direct product $\Gamma = \Gamma_Q \otimes \Gamma_R \otimes \Gamma_S$ of Hilbert spaces of three real spins of 1/2 *Q*, *R*, and *S*. The following eight states can be chosen as a basis for the Γ space:

$$|0\rangle = |000\rangle, \quad |1\rangle = |001\rangle, \quad |2\rangle = |010\rangle, \quad |3\rangle = |011\rangle,$$

$$|4\rangle = |100\rangle, \quad |5\rangle = |101\rangle, \quad |6\rangle = |110\rangle, \quad |7\rangle = |111\rangle,$$

where $|M\rangle = |m_Q, m_R, m_S\rangle$; e.g., $|5\rangle = |m_Q = +1/2, m_R = -1/2, m_S = +1/2\rangle$, etc.

Let us focus upon all possible gates based on the NOT operation. In a system of three spins, there are three NOT operations, viz., NOT on each spin with the unchanged states of the two other spins:

$$\mathrm{NOT}_Q = |1m_Rm_S\rangle\langle 0m_Rm_S| + |0m_Rm_S\rangle\langle 1m_Rm_S|,$$

$$\mathrm{NOT}_R = |m_Q1m_S\rangle\langle m_Q0m_S| + |m_Q0m_S\rangle\langle m_Q1m_S|,$$

$$\mathrm{NOT}_S = |m_Qm_R1\rangle\langle m_Qm_R0| + |m_Qm_R0\rangle\langle m_Qm_R1|.$$

One can next introduce six controlled-NOT operations CNOT. For example, if the state of spin *Q* is controlled by the state of spin *R*, then

$$\mathrm{CNOT}_{R\to Q} = |00m_S\rangle\langle 00m_S| + |11m_S\rangle\langle 01m_S| + |10m_S\rangle\langle 10m_S| + |01m_S\rangle\langle 11m_S|.$$

In the opposite situation,

$$\mathrm{CNOT}_{Q\to R} = |00m_S\rangle\langle 00m_S| + |01m_S\rangle\langle 01m_S| + |11m_S\rangle\langle 10m_S| + |10m_S\rangle\langle 11m_S|.$$

The CNOT operations for the *RS* and *QS* pairs are constructed in a similar manner.

Three CCNOT operations can also be introduced. For example, when the states of spin *S* are controlled by the states of *Q* and *R*, then

$$\mathrm{CCNOT}_{Q,R\to S} = |000\rangle\langle 000| + |001\rangle\langle 001| + |010\rangle\langle 010| + |011\rangle\langle 011| + |100\rangle\langle 100| + |101\rangle\langle 101| + |111\rangle\langle 110| + |110\rangle\langle 111|.$$

The CCNOT operations for the *Q* and *R* spins are constructed in a similar manner.

0021-3640/00/7107-0307$20.00

Virtual spin formalism. In the presently known NMR realizations of quantum gates, one-cubit NOT operation is accomplished through spin rotation by resonance rf pulses. Spin dynamics necessary for the two-qubit CNOT operation necessitates a two-particle spin–spin interaction [4].

However, quantum dynamics can be realized on a separate spin of 7/2 without invoking spin–spin interactions. It is also important that the CCNOT operation is realized by applying a single rf pulse. This can be implemented through a special information coding on the states of a spin of 7/2 using a virtual spin formalism suggested in [5].

A basis of the Hilbert $\Gamma_{7/2}$ space can be formed by the eigenfunctions χ_m of the $\mathbf{I}_z$ operator ($m = \pm 1/2, \pm 3/2, \pm 5/2, \pm 7/2$) or by the spin-energy eigenfunctions $|\psi_m\rangle$ defined below. Introducing notations $M = 0, 1, 2, 3, 4, 5, 6$, and 7 instead of the $|\psi_M\rangle = -7/2, -5/2, -3/2, -1/2, +1/2, +3/2, +5/2$, and $+7/2$ indices, one can set the $|M\rangle = |m_Q, m_R, m_S\rangle$ functions of virtual Q, R, and S spins of 1/2 into isomorphous correspondence to the $|\psi_M\rangle$ basis. Hence, to realize the above-mentioned gates, it is necessary to find a certain external action on a real spin of 7/2 such that the matrix of the evolution operator in the $|\psi_M\rangle$ basis coincides with the above expressions for the gates in the $|M\rangle$ basis.

Spin 7/2 and physical realization of gates. Let us consider the NMR spectrum of a nuclear spin $I = 7/2$ placed in a constant magnetic field H_0 and an axially symmetric crystal electric field:

$$\mathbf{H} = \mathbf{H}_z + \mathbf{H}_Q, \quad \mathbf{H}_z = -\hbar\omega_0\mathbf{I}_z,$$

$$\mathbf{H}_Q = (1/2)\hbar\omega_Q\Sigma_{\alpha = 0, \pm 1, \pm 2}Q_\alpha q_{-\alpha},$$

$$\mathbf{Q}_0 = \mathbf{I}_z^2 - I(I+1)/3, \quad \mathbf{Q}_{\pm 1} = \mathbf{I}_z\mathbf{I}_{\pm 1} + \mathbf{I}_{\pm 1}\mathbf{I}_z, \quad \mathbf{Q}_{\pm 2} = \mathbf{I}_{\pm 1}^2,$$
$$q_0 = 3\cos^2\theta - 1, \quad q_{\pm 1} = \sin\theta\cos\theta\exp(\pm i\varphi), \quad (1)$$
$$q_{\pm 2} = (1/2)\sin 2\theta\exp(\pm i2\varphi),$$

$$\omega_Q = 3e2qQ/[4I(2I-1)\hbar], \quad \mathbf{I}_{\pm 1} = \mathbf{I}_x \pm i\mathbf{I}_y,$$

where e is the electron charge; Q is the nuclear quadrupole moment; $\mathbf{I}_\beta$ ($\beta = x, y, z$) are the spatial components of the spin vector; $2eq$ is the absolute value of the electric field gradient; and θ and φ are the polar angles determining the orientation of its symmetry axis in the laboratory frame. To be specific, we consider the case when the quadrupole interaction is weaker than the Zeeman energy, so that its contribution can be treated perturbatively. Nevertheless, the quadrupole shifts are assumed to substantially exceed the widths of spin energy levels, so that the stationary NMR spectrum consists of seven well-resolved resonance lines spaced at frequency intervals on the order of quadrupole interaction ω_Q.

To a first approximation, the spin energy levels and eigenfunctions are

$$E_m \equiv \hbar\epsilon_m = -\hbar\omega_0 m + \hbar\omega_Q q_0(m^2 - 21/4),$$
$$|\psi_m\rangle = \chi_m + \Sigma_{m\neq k}\langle\chi_k|\mathbf{H}_Q|\chi_m\rangle/\hbar\omega_0(k-m)\chi_k. \quad (2)$$

Note that the normalization factor for the $|m\rangle$ function is omitted.

To simplify presentation, we write the spin operators through the projective operators $\mathbf{P}_{mn}$, which are represented by 8×8 matrices whose matrix elements p_{kl} are zero all except the $p_{mn} = 1$ element. The projective operators satisfy very simple conditions:

$$\mathbf{P}_{kl}\mathbf{P}_{mn} = \delta_{lm}\mathbf{P}_{kn}, \quad \mathbf{P}_{mn} = \mathbf{P}_{nm}^+,$$
$$\mathbf{P}_{mn}|\Psi_k\rangle = \delta_{nk}|\Psi_m\rangle. \quad (3)$$

Spin evolution under the action of an rf pulse inducing resonance transitions between the energy levels E_m and E_n ($E_m > E_n$) is described by the operator [5]

$$\mathbf{V}_X(\varphi_{mn}, f) = \mathbb{1} + (\mathbf{P}_{nn} + \mathbf{P}_{mm})[\cos(\varphi_{mn}/2) - 1]$$
$$+ i(\mathbf{P}_{mn}e^{if} + \mathbf{P}_{nm}e^{-if})\sin(\varphi_{mn}/2), \quad (4)$$
$$\varphi_{mn} = 2(t - t_0)\gamma H_{rf}|\langle n|\mathbf{I}_x|m\rangle|, \quad \mathbb{1} = \Sigma_m\mathbf{P}_{mm},$$

where it is assumed that the varying magnetic field is directed along the X-axis; H_{rf}, f, and $\Omega = \Omega_{mn} \equiv (E_m - E_n)/\hbar$ are its amplitude, phase, and frequency, respectively; and $\mathbb{1}$ is a unit operator in the $\Gamma_{7/2}$ space. After replacing f by $f + \pi/2$, expression (4) becomes valid for the Y-directed rf field.

Let us consider, in order of increasing gate complexity, how the information gates introduced above can be realized on the physical states of a separate spin of 7/2.

The CCNOT operation requires the application of one single-frequency pulse. For example, the $\mathrm{CCNOT}_{Q, R\to S}$ operation is accomplished by a pulse having frequency Ω_{67} and producing rotation at an angle of π. In this case, the evolution operator has the form

$$\mathbf{V}_X(\pi_{67}, 0) = \mathbb{1} - (\mathbf{P}_{77} + \mathbf{P}_{66}) + i(\mathbf{P}_{67} + \mathbf{P}_{76}).$$

Using the above-mentioned isomorphism, one can see, e.g., that the equality

$$\mathbf{P}_{67} + \mathbf{P}_{76} = |6\rangle\langle 7| + |7\rangle\langle 6| = |110\rangle\langle 111| + |111\rangle\langle 110|$$

holds. As a result, the evolution matrix $\mathbf{V}_X(\pi_{67}, 0)$ coincides, to a phase coefficient i of the nondiagonal operators, with the matrix of the $\mathrm{CCNOT}_{Q, R\to S}$ operation

$$\mathbf{V}_X(\pi_{67}, 0) = \mathrm{CCNOT}_{Q, R\to S}. \quad (5)$$

Likewise,

$$\mathbf{V}_X(\pi_{75}, 0) = \mathrm{CCNOT}_{Q, S\to R},$$
$$\mathbf{V}_X(\pi_{73}, 0) = \mathrm{CCNOT}_{R, S\to Q}. \quad (6)$$

Note that, unlike the resonance transition at frequency Ω_{67}, the transitions at frequencies Ω_{57} and Ω_{47} between

the χ_M states are allowed only to first order in the ω_Q/ω_0 parameter. Because of this, to accomplish rotation at an angle of π, the pulse duration or the rf field amplitude must be increased in these cases. Numerical calculations show that if the Zeeman and quadrupole energies are comparable, all necessary rotation angles involve matrix elements of the same order of magnitude.

The CNOT operation requires one double-frequency pulse. The corresponding evolution operator is a product of the following two operators:

$$\begin{aligned}
\mathbf{V}_X(\pi_{23}, 0)\mathbf{V}_X(\pi_{67}, 0) &= \mathrm{CNOT}_{R\to S},\\
\mathbf{V}_X(\pi_{13}, 0)\mathbf{V}_X(\pi_{57}, 0) &= \mathrm{CNOT}_{S\to R},\\
\mathbf{V}_X(\pi_{45}, 0)\mathbf{V}_X(\pi_{67}, 0) &= \mathrm{CNOT}_{Q\to S},\\
\mathbf{V}_X(\pi_{15}, 0)\mathbf{V}_X(\pi_{37}, 0) &= \mathrm{CNOT}_{S\to Q},\\
\mathbf{V}_X(\pi_{46}, 0)\mathbf{V}_X(\pi_{57}, 0) &= \mathrm{CNOT}_{Q\to R},\\
\mathbf{V}_X(\pi_{26}, 0)\mathbf{V}_X(\pi_{37}, 0) &= \mathrm{CNOT}_{R\to Q}.
\end{aligned} \tag{7}$$

The NOT operation requires one four-frequency pulse. Its evolution operator is a product of the following four operators:

$$\begin{aligned}
&\mathbf{V}_X(\pi_{04}, 0)\mathbf{V}_X(\pi_{15}, 0)\mathbf{V}_X(\pi_{26}, 0)\mathbf{V}_X(\pi_{37}, 0) = \mathrm{NOT}_Q,\\
&\mathbf{V}_X(\pi_{02}, 0)\mathbf{V}_X(\pi_{13}, 0)\mathbf{V}_X(\pi_{46}, 0)\mathbf{V}_X(\pi_{57}, 0) = \mathrm{NOT}_R,\\
&\mathbf{V}_X(\pi_{01}, 0)\mathbf{V}_X(\pi_{23}, 0)\mathbf{V}_X(\pi_{45}, 0)\mathbf{V}_X(\pi_{67}, 0) = \mathrm{NOT}_S.
\end{aligned} \tag{8}$$

Physical realizations (5)–(8) of the gates differ from the forms adopted in quantum informatics in that the nondiagonal projective operators contain phase multiplier *i*. This should be taken into account when constructing complex algorithms.

In the foregoing, the φ and *f* parameters in the formulas for evolution operators are specified in order to simplify presentation. Expressions (5)–(8) for the CCNOT, CNOT, and NOT gates can easily be generalized to the CCUT, CUT, and UT. For instance, if evolution operator (4) is taken with arbitrary parameters φ and *f*, then expression (5) for the CCNOT operator gives the expression for CCUT. The expressions for other logical operations can be obtained in a similar manner.

REFERENCES

1. T. Toffoli, in *Automata, Languages and Programming*, Ed. by J. W. de Bakker and J. van Leeuwen (Springer-Verlag, New York, 1980), p. 632.
2. D. Deutsch, Proc. R. Soc. London, Ser. A **425**, 73 (1989).
3. A. Barenco, C. H. Bennett, R. Cleve, *et al.*, Phys. Rev. A **52**, 3457 (1995); quant-ph/9503016.
4. D. G. Cory, M. D. Price, and T. F. Havel, Physica D (Amsterdam) **120**, 82 (1998); quant-ph/9709001.
5. A. R. Kessel' and V. L. Ermakov, Pis'ma Zh. Éksp. Teor. Fiz. **70**, 59 (1999) [JETP Lett. **70**, 61 (1999)]; quant-ph/9912047.

Translated by V. Sakun